




LENS-European Laboratory for Non-Linear Spectroscopy

Università degli Studi di Firenze

International Ph.D. "Atomic and Molecular Spectroscopy"

XXV CICLO

CHIM/02

---

Barbara Patrizi

# Dissociation and Geminate Recombination of CO in Truncated Hemoglobins Probed by Ultrafast Infrared Spectroscopy

---

Ph.D. Student: Patrizi Barbara

Tutor: Prof. Foggi Paolo

Coordinator: Prof. Pavone Francesco

---

2010/2013

*Dissociation and Geminate Recombination of CO in Truncated Hemoglobins Probed by Ultrafast Infrared Spectroscopy*

© 2013 by Barbara Patrizi

Ph.D. Thesis - LENS-University of Florence

Printed on January 2013

Cover: *Thermobifida fusca* truncated Hemoglobin

*To my family*

*To raise new questions, new possibilities, to regard old problems from a new angle, requires creative imagination and marks real advance in science.*

*Albert Einstein*

# Contents

Chapter 1

# Introduction

## 1.1 The Globin Superfamily

Till a few years ago, the definition of a globin was simply that of a protein resembling myoglobin (Mb) or the alpha and beta chains of hemoglobin (Hb). Based on DNA analysis of human and many other organisms, the globin family has expanded tremendously. The heme protein polypeptide chain is arranged around the prosthetic group, the heme, building up the so-called globin structure. The protein matrix determines the chemical environment of the active site and regulates its functional properties. The protein chain is linked to the heme through the interaction between the iron of the heme and the imidazole ring of the histidine residue located below the porphyrin ring, i.e. the proximal histidine. Heme is a chemically highly active group that has been involved in biological processes as soon as life appeared. Heme participates in many biochemical functions among which there are the binding and transport of gaseous ligands ($O_2$, NO, CO), the scavenging of free oxidant species, reactions of oxido-reduction and oxygen-sensing. To remain soluble and active it needs to be surrounded by a hydrophobic environment that is obtained by

a few structural 3D protein arrangements, the most common being the globin fold. The classical globin molecule is characterized by the canonical 3/3 alpha helical myoglobin fold, which has been described fifty years ago by Kendrew [1]. Myoglobin is characterized by a heme group surrounded by 8 helices designated A through H from the N to the C terminal. Helices A, B, C and E are on the distal site of the heme and helices F, G and H on the proximal site (Fig.1.1). In the last decade, hemoglobins were further described in some insects and as symbiotic hemoglobins (leghemoglobins) in the nodules of legume plants. Nonsymbiotic hemoglobins were also found in a large variety of plants other than legumes [2]. The emergence of high throughput genome sequencing facilities and powerful high performance bioinformatic tools allowed to reveal an unexpected wide occurrence of putative globin sequences in the three kingdoms of life. This led to a rapid growth of the globin superfamily. In all these molecules a similar 3D structure, characterized by the typical globin fold, has been found despite a large variety of functions and linear amino-acid sequences. Although the alignment of the amino acid sequences of globins from various sources reveals a high variability or even an almost random primary amino acid sequence, two key residues are conserved among all globin proteins encountered so far: Phe at position CD1 and His at position F8. Within this superfamily, a large group is made from globins, with sequences shorter than normal by 20 to 40 residues and named *truncated Hemoglobins* ($\mathrm{trHb}_s$). They were found in unicellular eukaryotes, [3], cyanobacteria [4], a nemertean [5], and a large number of bacteria [6, 7]. These globins are single domain molecules whose crystal structures exhibit an abbreviated 2/2 $\alpha$-helical fold characterized by a very short or absent A helix and a decreased CE inter-helical region. Most of the F helix occurs as a loop, with only helices BC, E, G and H left to surround the heme group. Globins longer than normal (more than 160 aminoacids) were observed in a green alga [8]

and in plants [9] with similar structural features. The discovery of hemoglobins in virtually all kingdoms of life has shown that the ancestral gene of hemoglobin was subjected to processes of deletions and insertions which have produced a large variety of new globins families. Amino acid sequence similarity between a mammalian globin and a bacteria globin may be less than 10% but the three-dimensional pattern defining the globin fold is well conserved.

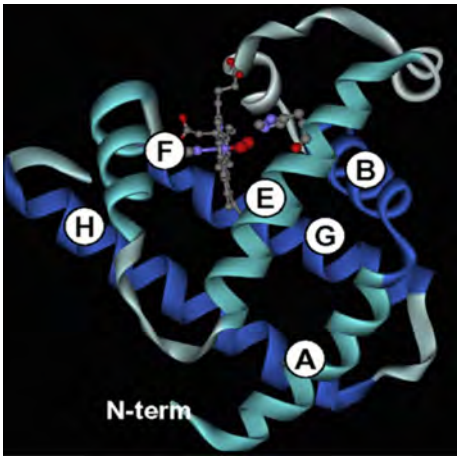


**Figure 1.1:** 3/3 $\alpha$-elical fold in Myoglobin. The heme group is surrounded by 3 helices on its proximal site (F, G, and H) and 3 helices on its distal site (A, B and E)[10].

## 1.2 Truncated Hemoglobins

Truncated Hemoglobins (trHb$_s$ or 2/2 Hb$_s$) [11] constitute a family of small oxygen-binding myoglobin-like proteins distributed in *eubacteria*, *cyanobacteria*, *protozoa*, and *plants* forming a distinct group within the Hemoglobin Superfamily. They are nearly ubiquitous in the plant kingdom, occur in many aggressively pathogenic bacteria, and are held to be of very ancient origin. Characteristically, trHb$_s$ occur at nano- to micromolar intracellular concentration, hinting at

a possible role as catalytic proteins. Crystal structures [12, 13] show that trHb$_s$ tertiary structure is based on a 2-on-2 $\alpha$-helical sandwich (Fig.1.2) as mentioned before. Moreover, an almost continuous hydrophobic tunnel, traversing the protein matrix from the molecular surface to the heme distal site, may provide a path for ligand diffusion to the heme.

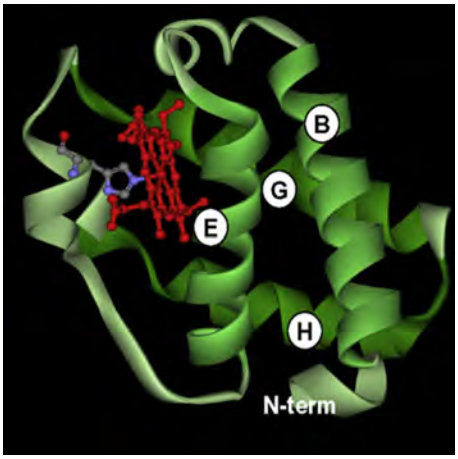


**Figure 1.2:** 2/2 $\alpha$-elical fold in *Chlamydomonas eugametos* hemoglobin, an example of a 2/2 Hb. Here the heme group is sandwiched between helices B and E on the distal site and helices G and H on the proximal site, helix F is reduced to a single turn in which a His residue (F8) is coordinated to the heme iron[10].

More than 40 putative trHb$_s$ genes have been identified. A phylogenetic analysis indicates that trHb$_s$ form a distinct family separate from bacterial flavohemoglobins, *Vitreoscilla* Hb, plant symbiotic and non-symbiotic hemoglobins, and animal hemoglobins. Three distinct groups (groups I, II, and III) can be distinguished within the trHb$_s$ family with four clusters within group II. The affiliation of each group depends on the internal sequence conservation. It is noticed that the patterns of amino acid conservation in the heme pocket of each of these groups differ from that of vertebrate or invertebrate 3/3 Hb$_s$ and that the sequence identity between trHb$_s$ from different groups

is lower than 20% of the overall identity, while it is very high within a given group. TrHb$_s$ from more than one group can coexist in the same organism, indicating a diversification of their functions. In this proteins the A-helix is drastically shorter, the D-helix is absent and an extended polypeptide segment (pre-F), followed by a short F-helix (one helix turn) is present. The helices are labelled according to the conventional globin fold nomenclature, A through H, starting from the N-terminal. Moreover, the C-D region is trimmed to about three residues, linking directly the C and E helices. Three Gly-motifs are individuated at the AB, at the EF inter-helical corners and just before the short F-helix. It has been suggested that this motifs contribute to the stabilization of the 2/2 fold, helping in locating the short A-helix onto the B and E helices. Besides the bend of H-helix, this one and the G-helix match the globin fold topology. One relevant difference between the three groups is the presence of the pre-F helix in group II. In fact, in group II the pre-F segment region hosts 15 residues, as the result of two amino acid insertions. This modification is reflected in the presence of a novel six-residue $\alpha$-helix (the $\phi$-helix), involved in interactions with the heme propionate [14]. The deviation of the pre-F segment relative to group I trHb$_s$ may be related to a significant shift of the whole heme group within the heme crevice of *Mycobacterium tubercolosis* trHbO (group II trHb$_s$). In group III 2/2 Hb$_s$ the A-helix is completely deleted, the AB hinge Gly-Gly motif is missing, thus forcing the protein residues preceding the B-helix to extend towards the GH region. An elongation of 7 amino acids is observed between the C and E helices. Such elongation of the CD region spans the C and E helices, but does not shift the position of the E-helix relative to the heme distal site. In all 2/2 globins, the fold establishes a scaffold sufficient to efficiently bury the heme group, and the hydrophobic residues at topological positions provide a network of Van der Waals contacts to the heme. Interactions between the heme and

polar residues are known to provide further stabilization; additional salt bridges link heme propionates and positively charged residues. The unique heme-protein covalent interaction has been revealed in the cyanobacterium Synechocystis sp. trHbN, occurring between the 2-vinyl group of the heme and a histidine residue [15]. A particular feature of this kind of proteins contrary to myoglobin of vertebrate is that, due to the shortened C-D region, the distal E-helix falls very close to the prosthetic group, thus causing side chain crowding of the distal site residues at topological position, such as B10, CD1, E7, E11 and G8. Some of these residues are polar, allowing the formation of a network of hydrogen bonds, functional to an efficient stabilization of the exogenous ligand, but also to the rebinding of dissociated ligands. The polarity of the distal residues is the common properties of the 2/2 $Hb_s$, but the residues involved in the building of the heme architecture switch over the three groups. In group I, for example, the hydrogen bond network involves residues at B10, E7 and E11 topological positions. The strongly conserved tyrosine (TyrB10) in position B10 plays a key role in the ligand stabilization through its OH group pointing directly to the heme ligand. Normally, the complete stabilization by hydrogen bond network is realized by a glutamine residue (Gln) located at E7 or E11, or at both positions. In group II, another residue, the tryptophan (TrpG8) is fully conserved; it contributes to the ligand stabilization through the formation of a hydrogen bond between the indole nitrogen atom and the ligand. Furthermore, the presence of a tyrosine at position CD1 in some $trHb_s$ proteins drastically modifies the interaction network. In particular, structure and sequence analysis suggests that the nature of residues at CD1 is correlated with the nature of the site E11, at least for the group II $trHb_s$. When the protein has a Tyr at CD1, a non polar residue is found at E11 position; conversely, when a non-hydrogen bond donor replaces the TyrCD1, a hydrogen bond donor is present in E11. TyrB10 and TrpG8 are invari-

ant residues also in group III trHb$_s$ and are directly hydrogen bonded to the ligand. Contrary to group II, the group III truncated proteins display an invariantly Phe residue in CD1 position and a hydrophobic residue at position E11 [16]. As a general feature of protein matrix, although the protein fold is simple and very well conserved, different routes for ligand diffusion to/from the heme may be coded: the group I 2/2 Hb$_s$ proteins show a cavity/tunnel system connecting the protein surface to the heme distal site, the group II 2/2 Hb$_s$ have a highly restricted protein matrix tunnel and finally, no evident cavity/tunnel system is present in the group III. It has been reported [7] that in the first group the tunnel is composed of two orthogonal branches from different access sites. Its potential role is thought to be the diffusion support and the accumulation of low polarity ligands/molecules. The residues lining the tunnels are generally hydrophobic. Instead, due to the different relative orientations of the helices and mainly to the increased volume of the side chains, the tunnel in group II is partially filled; in particular, the TrpG8 residue occupies the analogous volume of the shorter tunnel branch observed in group I, in the deeper part of the distal site pocket. The volume of the longer tunnel branch retains only two cavities, both fully shielded from bulk solvent. In order to better understand the links between the structure and the functionality of these proteins it is important to combine different techniques such as standard stationary spectroscopies and time-resolved spectroscopies. In this thesis, we focus our attention on two bacterial trHb$_s$ from *Thermobifida fusca* and *Bacillus subtilis* belonging to group II trHb$_s$.

## 1.3 CO as Probe of Heme Pocket Structure and Dynamics

In our experiments we used CO as a probe to study the recombination dynamics in two wild type trHb$_s$ from *Bacillus subtilis* and

*Thermobifida fusca* and its mutant 3F-*Tf*-trHb with Time-Resolved Infrared Spectroscopy (TRIR). The preference for CO arises from the fact that the protein-CO complex is spectroscopically easy clear to observe [17], its photodissociation quantum yield is equal to 1 [18] and the complex is easier to obtain than using $O_2$ or NO. Moreover the experimental investigated process is somehow opposite to the in vivo mechanism. In fact, the physiological cleavage of the iron-ligand bond occurs by thermal activation, the probability of the rebinding event strongly depends on the structure and dynamics of the protein chain. The impossibility of synchronizing the measurements with the arrival of external ligands in the near vicinity of the heme active site makes impossible to follow the direct conformational changes on the ultrafast timescale. Therefore, although the photodissociation is not a physiologically relevant event, it can be used to mimic the actual dynamics of the protein. In particular, the ultrafast processes triggered by the optical pulses are strongly related to the structure of the protein and to the protein-cofactor interactions [19]. The C-O stretching frequency has long been used as a monitor of structure and bonding in transition metal carbonyl complexes including CO adducts of heme proteins. Within the protein matrix the $\nu$(CO) stretching frequency of both heme-bound and dissociated CO are shifted by the internal electric field acting on the CO dipole; it diminishes for heme-bound CO by $\approx 200$ cm$^{-1}$ from its gas phase value of 2143 cm$^{-1}$ and falls in a region of the vibrational spectrum that is quite free from other molecular vibrations. $\nu$(CO) infrared intensity is augmented when an electric field is applied, infact CO stretching frequency for CO bound to the heme iron is a sensitive and anisotropic local detector of changes in the electrostatic field [20]. There is a linear correlation between the frequencies of the $\nu$(FeC) and the $\nu$(CO) stretching modes and this has been established and explained in terms of $\pi$ back-bonding of the Fe-CO unit. Back-donation from the Fe $d_\pi$ to

the CO $\pi^*$ orbitals increases the Fe-C bond order and decreases the C-O bond order, thereby increasing the $\nu$(FeC) stretching frequency and decreasing the $\nu$(CO) stretching frequency. The back-bonding is enhanced by many factors, such as steric hindrance of distal amino acids, increased polarity of the environment (positive charges) around the CO, and hydrogen-bonding between the CO oxygen atom and distal pocket residues. Moreover, the strength of the trans (axial) ligand has been found to affect the $\nu$(FeC) frequency; a weak or absent trans ligand increases this frequency due to a strengthening of the Fe-C$\sigma$ bond, whereas a strong trans ligand has the opposite effect [21]. Resonance Raman (RR) spectroscopy can monitor, at same time, $\nu$(FeC) and $\nu$(CO) vibrations, for this reason is a widely used technique for studying CO complexes of heme proteins [22]. Steric hindrance was thought to play an important role in determining the stretching frequency of bound CO however, studies on Mb mutants have suggested that the major factor governing $\nu$(CO) appears to be the electrostatic field surrounding the bound ligand and not steric hindrance [23, 24]. The Fe-CO bound states in myoglobin are called A states and are characterized by a series of closely spaced IR signals with the main band centered at maximum wavenumber of 1945 $cm^{-1}$. Native sperm whale Mb exhibits three A 'substates': $A_0$ at $\approx$ 1966 $cm^{-1}$, $A_1$ at $\approx$ 1945 $cm^{-1}$ and $A_3$ at $\approx$ 1933 $cm^{-1}$ [25]. Comparative studies of many distal mutants have shown multiple A substates originating from electrostatic interactions between the bound CO and different heme pocket environments. By analyzing various mutants of sperm whale and pig myoglobins Li et al. [24] found that electrostatic fields generated by polar distal pocket amino acids alter the electron distribution in the iron-carbonyl complex changing the order of CO bond and its IR stretching frequency. In contrast, bulky residues that cause marked decreases in CO affinity due to the steric hindrance have little effect on the IR spectrum. Changes in back-bonding result

from electron-donating or electron-withdrawing influences, either of porphyrin chemical substituents or of polar molecules in the vicinity of the bound CO. As a result, when CO is near a positively charged group, the $Fe^{+}{=}C{=}O^{-}$ tautomer is stabilized, in which the Fe-CO and C-O bonds have a double bond character, and the ligand oxygen has a partial negative charge. In contrast, when CO is near a negatively charged group, the $Fe^{-}{-}C{\equiv}O^{+}$ tautomer is stabilized, in which the Fe-CO bond leans toward a single bond character, and the C-O tends toward a triple bond character, whereas the ligand oxygen has a partial positive charge [26]. As mentioned in the previous section, in $trHb_s$ the distal site residues are very often polar and allow the formation of a hydrogen bonding network, which stabilizes the bound ligand by ehnancing the back bonding donation. In addition, to the $\nu$(CO) frequency, the IR spectrum can give informations about the direction of the transition moment via polarization measurements (see section 3.2.7). These kind of measurements have been carried out for MbCO and HbCO complexes using picosecond laser pulses by Moore and coworkers [27]. They studied iron-carbonyl geometries in carboxymyoglobin (MbCO) and carboxyhemoglobin (HbCO) using picosecond time-resolved infrared spectroscopy. Polarized infrared and visible beams were used to monitor the change in infrared absorbance of the bound CO stretch bands. The authors found an angle of 18 degrees for the 1951 $cm^{-1}$ band of HbCO; 20 degrees and 35 degrees, respectively, for the 1944 $cm^{-1}$ and 1933 $cm^{-1}$ bands of MbCO. Another crucial aspect is that since the vibrational transitions of free CO are sensetive to the chemical environment, it is possible to use the photodissociated ligand as a probe of the protein substates dynamics. Photodissociated CO trapped inside the protein matrix displays multiple IR bands around 2130 $cm^{-1}$ that are called B states; they arise from different locations and/or orientations of CO within the protein. In MbCO complex, within picoseconds af-

ter photolysis the ligand settles into an initial docking site B on top of the heme group, parallel to pyrrole C, where it resides for several nanoseconds before either rebinding or escaping to the solvent. It is well known [28] that the photodissociated ligand can either recombine rapidly with the metal or diffuse out into the solvent through the protein matrix. If the amino acids residues constituting the heme pocket confine the ligand near the metal, the *geminate recombination* (this expression refers to the reaction between two transient species produced from a common precursor before any separation by diffusion has occurred) takes place. If the ligand can easily diffuse away, and then comes back to the heme pocket, the *bimolecular recombination* takes place. After photodissociation, the diatomic molecules (initially bound to the ferrous iron) initiate a rapid migration away from the heme, and thereby probe the accessibility of the protein interior. In Mb and Hb, CO geminate recombination contributes only for a few percent to the total recombination at room temperature and occurs on the microsecond timescale and a few tens of percents on the tens of nanoseconds timescale [29], respectively. The dissociation of the ligand bound at the heme iron has been investigated for MbCO complex by means of femtosecond time-resolved infrared spectroscopy by Lim et al.[30] and two trajectories (state $B_1$ and state $B_2$) have been identified within a few hundreds femtoseconds that lead to CO located with opposite orientations. In both rotamers the CO axis ligand is roughly parallel to the heme plane. The authors assigned the high frequency (2130 $cm^{-1}$) $B_1$ state to the conformer with the O atom pointing back toward the heme iron atom and low frequency (2120 $cm^{-1}$) $B_2$ state to the other orientation on the basis of the kinetics of the appearance of the $\nu$(CO) bands after photolysis and the effect of isotopic substitution on the rate of recombination (Nienhaus and coworkers have made the opposite assignment on the basis of mutagenesis data, FT-IR spectroscopy and DFT calculations [31]). Both

B states features developed in less than 1 ps and the anisotropies corresponding to $B_1$ and $B_2$ evolved exponentially with time constant of 0.2±0.05 ps and 0.52±0.1 ps respectively converging to the same anisotropy at long times. It is useful to consider that the inertial rotation of gaseous CO at room temperature gives rise to a 0.1 ps decay of the polarization anisotropy. The two B states are kinetically and spectroscopically distinguishable. In particular, this two trjectories are spectroscopically distinguishable due to the vibrational Stark shift that arises from the electrostatic field surrounding the ligand. Furthermore, because the electrostatic field is inhomogeneous (non uniform in the three-dimensional space) the centre frequency of CO will be positioned depending on the orientation. Moreover, the authors [30] noticed that there was a net conversion from $B_2$ to the $B_1$ conformer and that the barrier against this exchange was small (3-4 Kj/mol) compared to that against recombination at iron (10 Kj/mol); this conversion seems to involve a simple rotation of the ligand about the center of the C-O bond [31]. Martin et al. [32] observed a progressive change in absorption strenght of the C-O between the heme bound and the docking site values (during its transfer from the heme to the docking site) by vis-pump mid-IR-probe spectrally integrated experiments. On the basis of DFT calculations they attributed this effect to the charge displacement from the heme iron to CO which affects the absorption strenght in a manner non linearly coupled to the vibrational frequency. This result implies that the CO vibrational absorption strenght is a suitable probe for the dynamics related to the ligand dissociation and transfer processes. In mammalian Mb, the highly conserved amino acid residues Val68, Ile107 and Leu29, in positions E11, G8 and B10 respectively, constitute the docking site. It has been shown [33] that the substitution of the latter with a phenylalanine strongly reduces the lifetime of the *docked* CO to 140 ps. Molecular dynamics simulation studies by Amadei, Di Nola and

coworkers [34, 35] have revealed the detailed kinetics of CO migration and binding in crystallized and solvated myoglobin. They showed that the CO motion and the protein fluctuations were strictly correlated. The final picture emerging from the previous and other studies [36, 37] is that ligands do not diffuse randomly but take preferred directions in moving away from the heme iron, ultimately reaching secondary well-defined sites that correspond to the Xe4 and Xe1 cavities of myoglobin [38]. For what concerns the ligand rebinding process it has been shown that slow geminate recombination may be the result of the stabilization of the ligand by interaction with amino acids in the pocket, as happens in the CO docking site in Mb. The distal barrier clearly depends on the enclosed amino acids residues and the trajectory of the dissociated ligand brings to collisions that vary with the protein motion fluctuations, thus influencing the rebinding kinetics. Although the geminate rebinding of NO with myoglobin is faster than those of $O_2$ and of CO [39], picosecond geminate recombination dynamics can be found also in the CO complex of many other proteins. Time-resolved CO rebinding studies were performed on microperoxidase, which consists of a heme with a proximal histidine that is part of an 11-peptide fragment [40]. This peptide is responsible of the solubility of the prosthetic group in water and, due to the fact that the peptide is not long enough to wrap around the heme, the photodissociated CO is exposed to the solvent and not to a closed docking site, as in Mb. The observed rebinding kinetics is not exponential, probably because the solvent cage effect influences the process. In this latter paper a model for the CO trapped within the solvent cage surrounding the heme is formulated and a kinetic time constant of $k = (110\ ps)^{-1}$ was estimated. It emerges that the rate of CO rebinding in this protein is much faster than in Mb; this suggests the idea that the presence of a docking site is responsible for the slow CO rebinding observed in most heme proteins. The geminate heme-CO recombination in heme pro-

teins is unusual; a chemically modified form of cytochrome c, termed carboxymethyl cytochrome c, is an example in which the recombination of CO is multiphasic with time constant of 16 ps, 120 ps and 1 ns [41]. The authors attributed these three phases to CO rebinding from different locations within the distal pocket region. The high efficiency of the CO rebinding was seen as the consequence of a sterically hindered 'caged' nature of the distal heme pocket from which it is difficult for CO to escape. It seems that the protein does not possess a ligand exchange pathway, in fact in cytochrome c the heme group is surrounded by a hydrophobic, structurally rigid pocket in which the interactions are weak. This configuration assures the restraint of the reorganization energy of the active heme environment, that guarantees the efficient electron transfer process. On the other hand, a structural flexibility of the protein chain is required in proteins where the ligand-transfer role is essential. Fascinating structural features for studying the ligand entry/escape dynamics to the active site (heme) are found in the recently discovered truncated hemoglobins. In the distal site of the heme pocket, the ensemble of polar residues are in contact with the iron-bound ligand coordination shell. Spectroscopic properties of CO in different wild-type and mutant adducts reveal that the oxygen atom of the heme-bound CO could be H-bonded to the indole nitrogen of tryptophan, the hydroxyl of tyrosine or the $NH_2$ group of glutamine. This common pattern has been defined 'ligand inclusive hydrogen bond network' [42, 43] and may represent a considerable barrier to ligand entrance and escape from/to the distal heme pocket. CO recombination has been recently studied in three $trHb_s$ namely the trHbO from *Mycobacterium tubercolosis*, the *Tf*-trHb from *Thermobifida fusca*, and the *Bs*-trHb from *Bacillus subtilis*. In the case of trHbO, using femtosecond spectroscopy, Vos and coworkers [44] have shown that CO rebinding occurs for 95% predominantly in 1.2 ns, indicating that the barrier for the ligand to escape to the solvent is

unusually high due to extremily high reactivity with the heme and/or that the ligand acces to the heme distal pocket is hindered by the network of aromatic residues and in particular by Trp88(G8). The unusually high reactivity of the ligand toward the heme in these class of globins would be linked to the rotational freedom of ligand in contrast with the situation observed for Mb in which the docking site forces the CO to lie parallel to the heme plane. Moreover, Vos and collegues [44] on the basis of molecular dynamics simulations have suggested a primary role for the structural water molecules present in the heme pocket of trHbO; this water molecules would retain the CO close to the heme iron at a distance favorable for ligand-heme bond formation by restricting the effective distal pocket volume. Furthermore they have noticed that CO rebinding is not drastically altered in case of substitution of Trp88(G8), and Tyr36(CD1) with Phe residues in single and double mutants of the wild type protein. All the mutant proteins have shown an additional decay phase of $\approx$ 250 ps not present in the wild type ptotein ($\tau_1$= 37 ps and $\tau_3$=1,2 ns) that would seem to indicate that changes in the strong hydrogen bonding network at the distal site yelds a more flexible heme pocket and a more heterogeneous environment for dissociated CO, but not strongly changing its reactivity towards the heme. Carbon monoxide geminate recombination in *Bs*-trHb has been reported to occour mainly with a time constant of 770 ps [43] indicating that even in this case the ligand is confined within the distal pocket with a remote possibility to escape to the solvent or to the adjacent small cavity located at the top of distal pocket. From this picture emerges that the active sites of *Bs*-trHb and trHbO are not designed to perform gaseous ligand exchange, but, maybe to perform redox processes involving oxygen or hydrogen peroxide. The complete CO recombination process in *Tf*-trHb from picoseconds to milliseconds has been very recently reported by Marcelli and coworkers [45]. The authors have used a combination of techniques such as

femtosecond transient absorption, nanosecond laser flash photolysis and optoacustic spectroscopy assisted by molecular dynamics simulations. As reported in the paper [45] photolysis of bound CO is followed by a rapid geminate recombination with a time constant of $\approx 2$ ns representing almost the 60% of the global reaction. An additional and small geminate recombination is also present at around 100 ns. As observed for the two proteins described above, even for *Tf*-trHb the large amplitude of the geminate phase suggests that the barrier for CO recombination is low and/ or the barrier for escape is high. The three proteins exhibit very similar heme pocket architecture with high conserved polar distal amino acids in contact with the iron-bound CO coordination shell responsible for the strong confinement of the dissociated ligand inside the protein matrix. For *Tf*-trHb nanosecond pholollysis experiments [45] have shown that first order processes are observed also on a longer time scale suggesting that photodissociated ligand may access transient docking sites located further from the distal pocket. The aim of this thesis has been focused on the study of CO geminate recombination dynamics in *Tf*-trHb (and its triple mutant3F-*Tf*-trHb) and in *Bs*-trHb by UV-Vis-Pump Mid-IR-probe spectroscopy in order to obtain additional pieces of information about ligand dynamics within the protein structure exploiting the molecular probe characteristics of the CO. For this reason we have also qualitatively compared the free CO stretching signals inside the three protein matrices with those of gaseous CO dissolved in organic solvents with different chemical-physical properties.

Chapter 2

# State of Art

## 2.1 *Thermobifida fusca* trHb

The identification of hemoglobin-like proteins in thermophilic actinobacterium *Thermobifida fusca* (*Tf*) was reported in 2005 [46]. The presence of hemoglobins in thermophilic micro-organism points out questions concerning the structural parameters that lead to thermostability of these proteins. Four genes within the genome of the bacterium *Thermobifida fusca* have been identified for as many proteins: a protoglobin (*Tf*-Pgb), a truncated hemoglobin (*Tf*-trHb), a flavohemoglobin (*Tf*-FHb) and an additional globin-like protein. The biochemical functionality and the physiological significance of these most interesting heme proteins are still unclear. The *Tf*-trHb is capable of efficient $O_2$ binding and releasing between 55 and 60 °C, the optimal growth temperature for *Thermobifida fusca*. On the contrary, vertebrate myoglobins are inefficient in exchanging exogenous ligands at high temperature. The crystal structure of the ferric, acetate-bound derivative was obtained at 2.48 Å resolution [46] and it is consistent to that of group II truncated hemoglobins. Its three-dimensional structure is reported in Fig.2.1 (PBD code: 2BMM): it

consists of a two-over-two alpha-helical structure.

**Figure 2.1:** *Thermobifida fusca* trHb structure obtained from the PDB file 2BMM [46]. The picture was generated with UCSF Chimera [47].

The distal heme pocket architecture (Fig.2.2) shows that the acetate ion ligand is stabilized by interactions with residues Tyr67 (CD1) and Trp119 (G8). The carbonyl oxygen of the acetate ion is hydrogen bonded to the OH group of the former amino acid and to the indole group of tryptophan (distances = 2.86 and 2.52 Å, respectively). The latter amino acid is rigorously conserved, i.e., in *Tf*-trHb and other two group II hemoglobins from *Mycobacterium tuberculosis* (*Mt*-trHbO) and from *Bacillus subtilis* (*Bs*-trHb). The Trp119 (G8) is essentially parallel to the heme plane. In the proximal region the His106-F8 is bonded to the Fe(III) of the heme at a short distance (N-Fe = 1.92 Å).

Some of the experiments presented in this thesis have been performed on a variant of the *Tf*trHb. This variant, called ASV (Acidic Surface Variant) differs from the Wild Type (WT) protein because both Phe107 and Arg91 are mutated to Glutamic acid to increase protein solubility , whithout affecting thermostability or ligand bind-

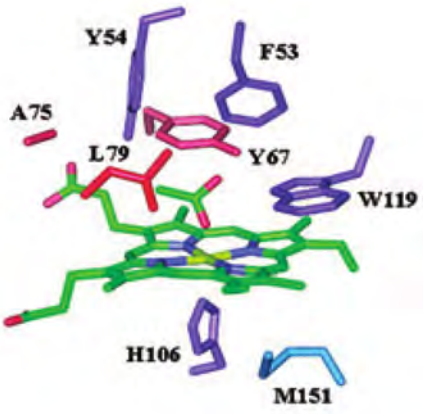


**Figure 2.2:** Close up view of *Thermobifida fusca* trHb heme pocket [46].

ing properties. The CO complexes of the WT protein and of the ASV variant have been characterized by infrared and resonance Raman spectroscopy. Two conformers have been identified: form 1 with $\nu$(FeC) and $\nu$(CO) at 509 and 1938 cm$^{-1}$ respectively, and form 2 with $\nu$(FeC) and $\nu$(CO) at 518 and 1920 cm$^{-1}$ respectively. CO interacts with Trp119 (G8) as single H-bond donor in form 1, whereas in form 2 is stabilized by two H-bonds in which both Tyr67 (CD1) and Trp119 (G8) are involved. The relevant role of H-bonding between CO and TrpG8 in the stabilization of both forms 1 and 2 has been highlighted by a study of site specific mutants of these residues (see next section)[48].

## 2.2 3F-*Tf*-trHb

The amino acidic residues of ASV variant have been modified through genetic engineering procedures [48] to study the effects of the substitution of the conserved amino acids inside the heme pocket. The final purpose is to better understand the role of these crucial amino acids

in the ligand rebinding process. For this reason, we performed experiments also on the triple mutant variant of the ASV protein in which the polar amino acids (TyrB10(54), TyrCD1(67) and TrpG8(119) have been replaced with Phe (Phenyalanine) residues. This variant is named Phe(YB10-YCD1F-WG8F) or 3F-*Tf*-trHb [48, 49] and the three dimensional structure of the distal heme pocket is shown in Fig.2.3. The structure has been determined with iron ligated to the acetate ion.

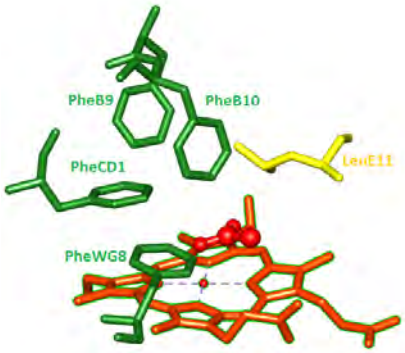


**Figure 2.3:** Three dimensional structure of the distal heme pocket of 3F-*Tf*-trHb. The PDB file was kindly provided by Prof. Alberto Boffi of the University of Rome 'La Sapienza' and the picture was generated with UCSF Chimera [47].

Carbon monoxide complexes of single, double and triple mutants of the ASV protein have been studied in a recent paper by Droghetti and coworkers [48]. In this work the ASV was used in a combinatorial mutagenesis of the distal heme pocket residues in which one, two, or three of the conserved polar residues [TyrB10(54), TyrCD1(67), and TrpG8(119)] were substituted with Phe. Mutants were characterized by infrared and resonance Raman spectroscopy and compared with the wild-type protein. Similar Fe-proximal His stretching frequencies have suggested that none of the mutations alters the proximal site of

the heme cavity. Instead, the spectra of the CO complexes have shown an extreme sensivity to the distal mutations. The back-donation from the Fe d$\pi$ to the CO$\pi^*$ orbitals is modulated by polar interactions and, in particular, by the formation of H-bonds between the bound CO and the distal protein residues. The electrostatic field generated by the polar distal pocket amino acids alters the electron distribution in the Fe-CO unit, changing the order of the C-O bond. The relevant role of H-bonding between CO and TrpG8 in the stabilization of both forms 1 and 2 has been highlighted studying site specific mutant proteins of these topic residues. Upon mutation of TrpG8 to Phe (WG8F mutant), the vibrational spectra change substantially: two $\nu$(FeC) bands are observed at 491 and 497 cm$^{-1}$ and two $\nu$(CO) bands at 1962 and 1942 cm$^{-1}$. The spectra of the single mutants YCD1F and YB10F confirm the assignment of forms 1 and 2 to a single CO-TrpG8 interaction and a double CO-TrpG8/CO-TyrCD1 interaction, respectively. This lead the authors to conclude that CO in the latter case is surrounded by an environment similar to that of the native protein. On the other hand, a very strong effect is exerted by the YCD1 mutation, because only one conformer (the less polar one) survives in YCD1F mutant. The double variant YCD1F-WG8F behaves like the WG8F single mutant: being characterized by two $\nu$(FeC) bands at 488 and 498 cm$^{-1}$ and two $\nu$(CO) bands at 1952 (very weak) and 1967 cm$^{-1}$. Only one apolar form $\nu$(FeC) at 494 cm$^{-1}$ and $\nu$(CO) at 1955 cm$^{-1}$ instead is observed in the case of the triple Phe mutation in the mutant YB10F-YCD1F-WG8F. For a complete view see Fig.2.4. In the latter protein the hydrogen bonding network is completely removed and CO is not stabilized by the formation of H-bonds.

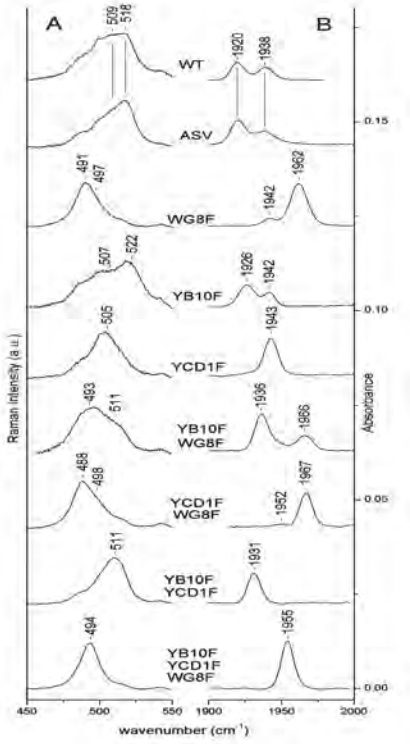


**Figure 2.4:** RR spectra (left) obtained with an excitation wavelength of 413.1 nm and IR spectra (right) of the CO complexes of native and mutated ferrous *Tf*-trHb variants at pH 7.0. Picture taken from Ref.[48].

## 2.3 *Bacillus subtilis* trHb

The genes encoding for truncated hemoglobins have been identified in all species of the *Bacillus* genus, including *Bacillus subtilis*. In all *Bacillus* species , whose genomes have been sequenced, truncated hemoglobins coexist with true-type heme-containing chemotactic oxygen sensors and flavohemoglobins. Moreover, in *Bacillus subtilis* the globin-like sensor domain of the HemAT (Heme-based Aerotactic Transducer) oxygen sensor as well as the flavohemoglobin domain share little sequence similarity with the $trHb_s$. Structural alignments reveal

that key residues within the heme pocket are not conserved, suggesting different functional roles for the three proteins [50]. The ferric, cyanide-bound derivative of this protein was obtained at 2.15 Å resolution [51] and the relative three-dimensional structure is reported in Fig.2.5.

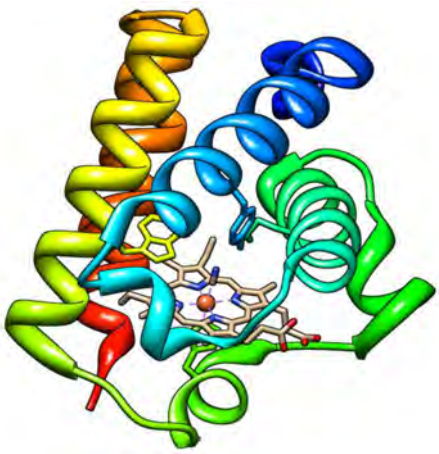

**Figure 2.5:** Stereoview of *Bacillus subtilis* trHb (PDB code: 1UX8)[51]. The picture was generated with UCSF Chimera [47].

The distal heme pocket of *Bs*-trHb is characterized by the presence of polar residues surrounding the bound ligand, namely Tyr25 (B10), Thr45 (E7), and Gln49 (E11) (Fig.2.6). The cyanide ion is almost perpendicular to the heme plane, and the carbon atom is bound to the ferric heme iron at a distance of 1.92 Å. The cyanide ion is stabilized mostly by the Tyr25 (B10) residue, which is hydrogen-bonded through the OH group directly to the cyanide nitrogen atom (distance=2.54 Å). Trp89 (G8) is buried in the distal pocket and is roughly parallel to the heme plane with the indole NE1 atom placed at a distance of 3.4 Å from the cyanide nitrogen atom. At the external edge of the distal site, a Lys residue, Lys48 (E10), forms a salt bridge with the heme propionate D. This salt bridge is on the external surface of the

protein and may hinder access to the distal pocket. Most interestingly, position E10 is occupied by a positively charged residue in all three groups of trHb$_s$. The position and orientation of the proximal histidine is typical of an unstrained imidazole ring that facilitates the heme in-plane location of the iron atom. Although the unconstrained histidine conformation appears to be a common feature of the trHb$_s$ investigated to date [52] and the coordination bond formed by His76 (F8) is stronger than in other hemoglobins as indicated by the unusually short iron-histidine distance (N-Fe(III)=1.91 Å).


**Figure 2.6:** Close up view of the active site of *Bacillus subtilis* trHb (PDB code: 1UX8)[51].

It is of interest that in *Bs*-trHb the proximal pocket appears to be directly exposed to solvent through a 55-Å$^2$ aperture situated in a shallow depression delimited by the phenyl ring of Phe79, the carbonyl backbone portion of Arg75 (F7), and the heme propionates. The center of the depression is occupied by spurs formed by the positively charged residues Arg75 (F7), whose $NH_2$ is hydrogen-bonded to the main chain oxygen (distance=2.84 Å) of His69, and Lys48 (E10) that forms a salt bridge with the oxygen atom of the heme propionate D.

Two major cavities can be identified in *Bs*-trHb, the inner cavity is lined by residues Val21 and Phe24 on the B-helix, Gln49 and Leu53 on the E-helix, and Trp89 (G8) and Met93 on the G-helix, whereas the more external one is lined by residues Tyr56 and Leu57 on the C-terminal part of the G-helix and by Phe109, Leu110, and Arg113 on the H-helix. The passage between the two cavities is blocked by Tyr56, Leu53, and Leu114. *Bs*-trHb-CO complex has been characterized by Feis et al. [43]. Accordingly, in both resonance Raman and IR spectra two bands corresponding to $\nu$(CO) stretching modes were identified at 1925 and 1888 $cm^{-1}$. On the basis of the intensities and frequencies of the bands, two different conformers of the *Bs*-trHb-CO complex have been observed: form1 characterized by $\nu$(FeC) at 545 $cm^{-1}$, $\delta$(FeCO) at 589 $cm^{-1}$ and $\nu$(CO) at 1888 $cm^{-1}$, which corresponds to CO H-bonded to both TyrB10 (Tyr25) and TrpG8 (Trp89), and form 2, characterized by $\nu$(FeC) at 520 $cm^{-1}$ and $\nu$(CO) at 1925 $cm^{-1}$ which corresponds to CO single H-bonded to TyrB10 (Tyr25). The very low C-O stretching frequency at 1888 $cm^{-1}$ (corresponding to the extremely high RR stretching frequency at 545 $cm^{-1}$) indicates an unusually strong hydrogen bonding between CO and distal residues. Feis and coworkers [43] have also demonstrated that mutation on of Trp89 (G8) to Leu deeply alters the hydrogen bonding network giving rise to a conformer in which the predominant features are a Fe-CO stretching band at 489 $cm^{-1}$ and a CO stretching band at 1958 $cm^{-1}$.

## 2.4 The Heme Group

The biological activity of heme proteins depends in part from the structural properties of heme group. It is well known that heme is of considerable biological importance, being the active centre for ligand binding, electron transfer and catalytic activity. The fact that heme group can play such diverse roles in biology is a clear testi-

mony of the fact that the protein matrix has a strong influence on its chemical properties. Several biologically different types of heme exist, the most important is the heme b (or protoporphyrin IX). The heme proteins studied in this thesis contain heme b. The heme contains one iron atom coordinating the nitrogens of the protoporphyrin IX in the equatorial positions (Fig.2.7). The protoporphyrin IX is a tetrapyrrole macrocycle containing different peripheral substituents: two vinyl groups in positions 2 and 4, four methyl groups in positions 1, 3, 5 and 8 and two propionyl chains in positions 6 and 7. The iron can assume two stable oxidation state, the ferric ($Fe^{3+}$) and ferrous ($Fe^{2+}$) forms. Whereas free iron-protoporphyrin IX adopts a planar structure, the protein matrix can exert constraints that diminish the planarity of the chromophore.

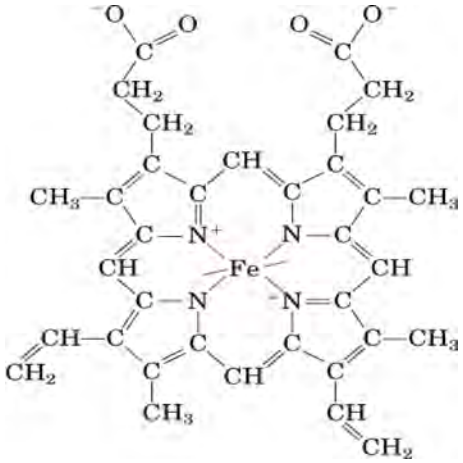

**Figure 2.7:** Structure of Fe-protoporphyrin IX.

### 2.4.1 Electronic Absorption Spectra of Heme and Heme proteins

The optical properties of the iron-protoporphyrin IX complexes have been studied since many years [53] and are considered deriving from the highly conjugated $\pi$ electron system. Two electronic transitions

(giving rise to B and Q bands) dominate the UV-Vis region of the absorption spectrum of iron-porphyrin complex, that correspond to the porphyrin $\pi \rightarrow \pi^*$ singlet transitions. The B band corresponds to the $a_{1u} \rightarrow e_g$ transition and the Q band to the $a_{2u} \rightarrow e_g$ transition (Fig.2.8).

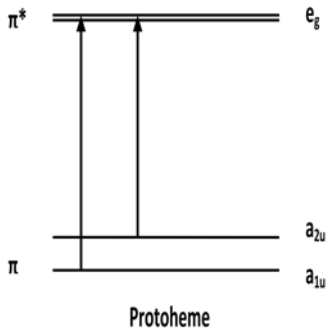


**Figure 2.8:** The orbital diagram of protoheme proposed by Gouterman [53].

There is a strong interaction between these two transitions, so that the transition dipoles are summed for the intense B band (also called Soret) and nearly cancelled for the Q band. Some intensity is regained by the Q transition via vibronic mixing, giving rise to the $Q_0$ ($\alpha$) band and its vibronic envelope, $Q_V$ ($\beta$) band. When the conjugation of the porphyrin ring is extended to the vinyl groups the energy of the Q and B transitions is lowered and consequently the absorption bands can be red shifted by 4-10 nm, depending on the degree of conjugation between the porphyrin aromatic system and the vinyl double bonds [54]. Applying the Huckel approximation method, Gouterman discovered an interaction between the $\pi$ orbitals of the porphryn and d orbitals of the iron, due to their comparable energetic levels and favourable symmetry [55]. Therefore, information about

the oxidation, the spin and the coordination states of the heme iron can be obtained by analyzing the wavelength of the Soret, $\beta$ and $\alpha$ bands in the UV-Visible spectra. In fact, ($Fe^{2+}$) has six valence electrons in its 3d orbitals while ($Fe^{3+}$) has five valence electrons. The two axial positions of the iron atom can be occupied by ligands and they could introduce an external perturbation. If the interaction with ligands is weak or the sixth position is not occupied, the d orbitals are quasi-degenerate and the occupancy follows the Hund's rule, thus producing a high spin (HS) configuration: S = 5/2 for ($Fe^{3+}$) and S = 2 for ($Fe^{2+}$). On the other hand, a strong interaction with the ligands can alter the relative energies of the 3d orbitals removing their degeneracy (the well-known process of ligand field splitting) and producing a low spin (LS) configuration. In this case the two 3d orbitals that point directly to the approaching ligands, i.e. the $dz^2$ and the $dx^2$-$dy^2$ are lifted in energy above the remaining three 3d orbitals ($d_{xy}$, $d_{xz}$ and $d_{yz}$), and the electrons occupy only the lower orbitals generating the configuration S = 1/2 for ($Fe^{3+}$) and S = 0 for ($Fe^{2+}$). Since in the LS configuration the higher energy orbitals are unoccupied, the size of the core containing the iron atom is smaller than in the HS configuration and the metal lies in the plane of the tetrapyrrole ring, while the HS iron sits out of plane. Furthermore, an extra band at longer wavelength (in the 600-700 nm region) is observed only for high-spin (HS) $Fe^{3+}$ heme proteins, assigned to a charge-trasfer transition (CT1) from the porphyrin to the iron orbitals [$a_{2u}(\pi) \rightarrow e_g(d_\pi)$] (Fig.2.9). The intensity and the wavelength of the CT1 band are related to the energy difference between the d orbitals of the metal and the $\pi$ orbitals of the porphyrins, which in turn, depend on the nature of the axial ligands.

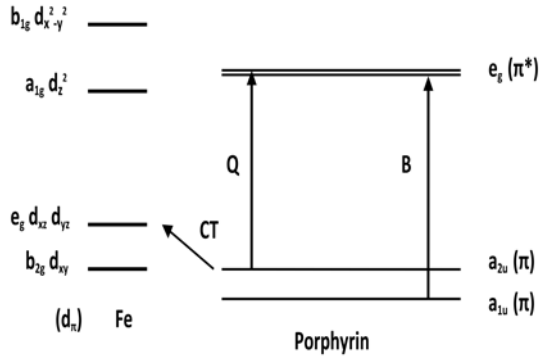


**Figure 2.9:** Scheme of the electronic transitions observed in a heme protein. On the left are reported the energy levels for the iron atom, on the right the energy levels for the protoporphyrin are shown.

### 2.4.2 Photophysics of Heme proteins

The first studies on fast processes in heme proteins were performed essentially on the mammalian model oxygen storage and transport proteins Myoglobin and Hemoglobin. The absorption of a photon by the heme lead to a series of sub-nanosecond processes among which the formation of transient excited electronic states with the subsequent structural response of the macrocycle to the new electronic configuration, and the nonradiative relaxation to the ground state. Photophysical behavior of metalloporphyrins in solutions were extensively studied [56, 57, 58], the results have shown that a number of various electronic states are involved in the relaxation process. The first experiment dealing with excited state relaxation and photolysis in heme proteins by means of subpicosecond optical pulses, was reported in 1976 [59]. Photodissociation of carboxyhemoglobin (HbCO) was found to occur in less than 0.5 ps. The authors argued that the HbCO is easily dissociated because there is a radiationless transition

from the initially excited electronic state of the porphyrin $\pi$-electrons to a lower state corresponding to a $d_\pi \rightarrow d_{z^2}$ excitation of the iron atom. Contrary to $d_\pi$, the $d_{z^2}$ orbital has a partially antibonding nature, which results in a repulsive force exerted on the CO molecule. An induced absorption was also observed; in the unliganded ferrous hemoglobin and oxyhemoglobin, the signal decays rapidly with a time constant of about 2.5 ps, while in HbCO it remains unchanged on a timescale of 20 ps. The observed response was interpreted as the evidence of a short-lived excited state. This experiment was carried out using pulses at 615 nm for excitation and probing and it was not possible to identify the nature of such state. In subsequent experiments was observed that the photolysis of HbCO brings to a broader, weaker and red-shifted signal compared with the steady-state spectrum of the deoxygenated ferrous Hb species. By means of extended Hückel calculations performed on the complex of iron-porphine with imidazole as a model chromophore, a detailed assignment of the transitions in the hemoglobin and its adducts were reported by Eaton et al. [60]. In the early 1980s, femtosecond photolysis experiments in CO ligated Mb and Hb, along with the CO adduct of protoheme were carried out [39, 61]. The results showed that deoxy species appeared after 350 fs, i.e. the formation rate was identical for the three molecular species and independent of the presence of the protein chain. The authors concluded that the instantaneous formation of a transient high-spin ligated, highly photodissociative species relaxed to a stable high spin pentacoordinated state with out-of-plane displacement of iron. In other words, they suggested that the photodissociative species in heme-CO complexes is a low-lying multiplet ligand field state, populated via intersystem crossing. For the three molecules, an identical time constant of 3.2 ps was also observed and interpreted as the relaxation time of the directly excited ligated state towards the non-reactive ground state. In ordrer to obtain detailed information

on the dynamics of the heme and of discriminating the energy dissipation processes after photoexcitation from the structural relaxation, a Raman spectrometer providing, at the same time, both subpicosecond resolution and independently tunable pump and probe pulses was developed [62]. The obtained results are reported in a review by J.L. Martin and M. H. Vos [19]. They concluded that in hemoprotein dynamics, the photodissociation of the ligand occurs in less than 50 fs with a quantum yield of approximately unity, indifferent of whether the ligand is CO, $O_2$ or NO, and that two short-lived species are formed upon ligand photodissociation. By following the kinetics of the transient bleaching of the Soret band after photoexcitation in the Q band, Martin and coworkers assigned these transients to excited states of the unligated heme and labelled them $Hb^*_I$ and $Hb^*_{II}$. The first was attributed to the transient species in which the heme is already partially domed and that decays in 300 fs to the ground state unligated species. The second was found to relax in 2.5-3.2 ps and the weight of this component was strongly dependent on the nature of the ligand, in particular it was found to be very low for the CO adduct. On the basis of experimental observations, the relaxation process was attributed to a homogeneous distribution of ligands in the heme pocket that rapidly recombine with heme. The fast recombination suggested that the heme in $Hb^*_{II}$ does not change from the planar geometry of the ligated initial ground state and that the relative population is responsible for the geminate recombination of the ligand. Moreover, due to the similarities of the noticed protoheme behavior with those of heme proteins, the authors agreed that the steric features of the protein are less important than the nature of the ligand itself in determining the geminate recombination process. Moreover the authors suggested an alternative assignment for the two transient species $Hb^*_I$ and $Hb^*_{II}$. Both of them might be attributed to vibrationally hot ground state unligated hemes. However, they con-

sider the two states as electronic excited states because of the large frequency different between their absorptions and the ground state Soret band; in fact, the latter was known to be relatively insensitive to temperature. This model is one of first proposed, more recently it has been corrected [63]. The previous parallel model, was replaced by a sequential model where the photoexcited heme decays to an intermediate state called $Hb^*_I$ through a metal-to-ring ultrafast charge transfer($\approx$ 50 ps). Subsequently, the $Hb^*_{II}$ state arises from $Hb^*_I$ via porphyrin-to-iron back charge transfer to produce a porphyrin ground state configuration and a non-equilibrium iron d-orbital population. So the $Hb^*_{II}$ state was assigned to a vibrationally excited ground state macrocycle with a d-$d^*$ excited metal ion center. This sequential model can be summarized as:

$$^1\mathrm{Q} \rightarrow Hb^*_I \rightarrow Hb^*_{II} \rightarrow Hb.$$

$Hb^*_{II}$ is formed from $Hb^*_I$ in less than 300 fs; its decay to the heme ground state occurs in about 3 ps. The proposed pathway suggests also that the metal-to-ring ($d_\pi \rightarrow a_{1u}$, $a_{2u}$) charge transfer is the key event in the mechanism of photolysis of diatomic ligand following a porphyrin ring $\pi \rightarrow \pi^*$ transition. Another sequential model was discussed in 2000 by Kholodenko et al [64]. They detected two steps of electronic relaxation: a sub 100 fs step, seen as an instrument limited spike, and one with a time constant of a few hundred femtoseconds. After this second step, Mb is in a vibrationally hot, thermally non-equilibrated, ground electronic state. The vibrational relaxation shows a non-exponential behavior, that was fitted by a two exponential function, with a short time constant of a few ps and a second one, of smaller amplitude, of about 15-20 ps. The first time constant was related to the fast initial dephasing process due to the IVR (Intramolecular Vibration Redistribution), while the second was attributed to a slower cooling process associated to the VR (Vibrational Relaxation) from the heme to the solvent through the protein

backbone. The dynamics observed in the picoseconds temporal range was then ascribed to the vibrational cooling in the ground electronic state. Lim et al [65] have proposed an intermediate picture for the process following the photoexcitation of myoglobin, in which contributions from both electronic and thermal relaxation are involved on the picosecond timescale. In fact, they found that the electronic relaxation to the ground state is not instantaneous (exponential growth time constant of 3.4 ± 0.4 ps), but proceeds through several intermediate electronic states, while the temperature of the electronically relaxed heme cools with a single exponential time constant of 6.2 ± 0.5 ps. From the theoretical point of view, many papers have to be mentioned [66, 67, 68, 17, 69]. Their results confirm the assignment of the first intermediate state as an iron-to-ring charge transfer state, ruling out the possibility of an involvement of a high spin state in the photodissociation step. Although the analysis of data reported by Franzen et al [63] intends to resolve the contradiction between the previous different interpretations [62, 64, 65], the photophysical model of the relaxation processes in heme proteins can not be consider certain yet. In 2003, Ye and coworker published the results of their research on ferric and ferrous myoglobin, proposing an interpretation based on the vibrationally excited (*hot*) electronic ground-state model [70]. Independently from the oxidation and ligation states, the spectra show an initially broad and red-shifted transient absorption signals which eventually decay to a typical band profile of a thermally relaxed state. Two components of the spectral evolution were discussed, involving both intramolecular, non-Boltzmann, vibrational redistribution (less than 1 ps) and cooling of a hot, Boltzmann equilibrated heme via vibrational energy transfer from the heme to the protein/solvent heat bath. Their discussion was based on the time evolution of specific spectral features; in particular, the authors observed on the blue side of the Soret band a component that could not

be adequately explained. Under this respect the multiple electronic intermediate excited-state model results incorrect. They compared their point of view with the work published in 1988 by Petrich et al., stressing that the model proposed by Petrich et al. was based only on single wavelength measurements. To tell the true, their discussion omitted any confrontation with the sequential model of Franzen et al., cited above. It was only enumerated as an example of multiple electronic state models. In conclusion, different models have been proposed for the interpretation the ultrafast heme dynamics and for the nature of the short lived intermediates generated immediately after photolysis. Although the role of low-lying electronic excited state and of vibrational energy relaxation in the heme time evolution after photo-excitation represents a key point of the current research on hemoprotein dynamics and is currently subject of debate.

Chapter 3

# Spectroscopic Techniques, Experimental Details and Data Analysis

## 3.1 Ultrafast Spectroscopy and the Birth of Femtochemistry and Femtobiology

The application of femtosecond light pulses in chemistry and biology has created new fields of research, such as *femtochemistry* and *femtobiology* [71]. Their development is linked to such femtosecond pulse properties as short duration, significant spectral width and high peak intensity. These properties have determined new directions of research, making possible to obtain previously unavailable informations. The dynamics of elementary physical and chemical processes can be followed in real time by femtosecond pump-probe spectroscopy. Ultrafast spectroscopy has played and plays an important role in the study of a number of biological processes and it has provided unique pieces of information about several of nature's responses to light. Molecular systems with biological function are generally very complex and

the reactions constituting the biological function are frequently ranging from the most elementary chemical reactions to processes implying large-scale molecular motions or transformations. The primary steps of biochemical processes take place within proteins and protein complexes. Redox changes, conformational transformations and local structure rearrangements induced by ligand binding may occur on a femtosecond time scale, after external triggering. These changes result from long-distance interactions, which are characteristic for proteins. Ligand dissociation-association in heme proteins is a typical example. The development of femtosecond laser spectroscopy and its direct application by biophysicists in the past ten years has been crucial in understanding ultrafast processes in biological systems [72]. In transient absorption spectroscopy, a fraction of the molecules is promoted to an electronically excited state by means of an excitation (or pump) pulse. A weak probe pulse is sent through the sample with a delay $\tau$ with respect to the pump pulse. A difference absorption spectrum is then calculated, i.e., the absorption spectrum of the excited sample minus the absorption spectrum of the sample in the ground state ($\Delta$A). By changing the time delay $\tau$ between the pump and the probe and recording a $\Delta$A spectrum at each time delay, a $\Delta$A profile as a function of $\tau$ and wavelength $\lambda$, i.e., a $\Delta A(\lambda, \tau)$ is obtained. $\Delta A(\lambda, \tau)$ contains information on the dynamic processes that occur in the system under study. A pump-probe pulse sequence allows to obtain an excited state absorption spectrum at a certain delay time. By repeating this sequence as a function of the pump-probe delay, it is possible to obtain the dynamical evolution (kinetics) of the transient absorption signal.

## 3.2 Time Resolved Infrared Spectroscopy

In TRIR experiments, a photoinduced reaction is initiated by femtosecond UV-Vis pump pulses, and the dynamics of the system are followed by probing the induced changes of transmission of a sample with femtosecond mid-IR pulses. Laser technology makes it possible nowadays, to generate stable femtosecond pulses shorter than 100 fs, tunable in a wide infrared spectral range covering the region between 1000 $cm^{-1}$ and 10000 $cm^{-1}$. The technology of femtosecond IR spectroscopy has progressed to the point where the accessible time resolution is significantly shorter than the typical dephasing times of vibrational transitions. TRIR is a suitable technique for the study of ligand-protein interactions in heme proteins. After an optical 'pump' pulse triggers the process to be studied, the 'probe' records the time-dependent changes in the IR spectrum. Because many different types of vibrational modes are resolved in proteic systems, IR spectroscopy can monitor functional groups in a highly specific manner. Moreover, the vibrational frequency and widths of these infrared bands are often very sensitive to environmental change, thereby providing incisive probes of the reaction pathway. Specific targets include amide I band (1600-1700 $cm^{-1}$), which arises primarily from carbonyl stretching modes along the protein backbone. Because the backbone C=O stretch is highly sensitive to hydrogen bonding, it is a useful marker of secondary and tertiary structure [73]. Similarly, the sensitivity of the cysteine S-H stretch to hydrogen bonding has been exploited as a probe of both tertiary and quaternary conformation in hemoglobin [74]. Moreover, IR probes of cofactors allow one to directly study cofactor-protein interactions. The ability to probe infrared-active ligands such as CO, NO, and CN has facilitated the study of ligand-protein interactions in heme proteins. In particular, the strong IR absorption of CO affords an ideal probe of ligand dynamics in proteins and it represents, even in our case, a unique tool to investigate

recombination dynamics in the trHb$_s$ by Uv-Vis Pump/Mid-IR Probe spectroscopy.

Pump-probe spectroscopy is a third-order nonlinear technique, where a third-order polarization $P^{(3)}(t)$ is generated in the sample by two interactions with the pump and one interaction with the probe field. The polarization acts as a source term in the Maxwell equations, which can be solved in the slowly varying envelope approximation and the small signal limit[75]. In this approximation the wave equation connecting polarization and electric field is given by:

$$\frac{\partial E(t)}{\partial z} = \frac{i\omega_{pr}}{\varepsilon_o c} P(t) \tag{3.1}$$

which in the small signal limits gives the solution

$$E_{pr,Tot}(t) = E_{pr}(t) + E_{Gen}(t), \quad E_{Gen}(t) = \frac{i\omega_{pr} L}{\varepsilon_o c} P(t) \tag{3.2}$$

where L is the optical path length of the sample. Hence, the polarization $P$ of the sample generates a new pulsed field, $E_{Gen}(t)$, which interferes with the original probing field $E_{pr}(t)$ on the detector. Transient gain or absorption corresponds to a generated field which is in-phase or out of phase with the probe field. In general, the detector will be slow compared to the duration of the femtosecond pulses. Thus, the total signal detected is proportional to the time integral of the light intensity, resulting in:

$$\int_{-\infty}^{+\infty} dt\, |E_{pr,Tot}(t)|^2 = \int_{-\infty}^{+\infty} dt\, \Big[ |E_{pr}(t)|^2 + |E_{Gen}(t)|^2 + 2\mathrm{Re} E_{pr}(t) E_{Gen}(t) \Big] \tag{3.3}$$

where the first term is constant, and can be subtracted off in an experiment through proper normalization, the second term will be negligibly small (in the small signal limit), and the third term contains

the relevant information on the nonlinear polarization generated in the sample. In the case of spectrally resolved detection, the measured signal (spectrally resolved transmission change) is then given by:

$$\frac{\Delta T(\omega)}{T_0(\omega)} = \frac{T(\omega) - T_0(\omega)}{T_0(\omega)}$$

$$\frac{\Delta T(\omega)}{T_0(\omega)} \quad \omega \mathrm{Im}\left[\frac{P^{(3)}(\omega)}{E^*_{pr}(\omega)}\right] \tag{3.4}$$

where $T(\omega)$ and $T_0(\omega)$ are the transmission of the sample with and without excitation, and $E_{pr}(\omega)$ is the Fourier transform of the time dependent probe field. It follows from this expression that not only population changes contribute to the pump-probe signals, but also coherent polarizations. The impulsive excitation process creates coherent, non stationary superpositions of states (wavepackets) in the system. Only after the decay of coherence is completed, a description in terms of population dynamics is appropriate. Coherence is destroyed by dephasing processes, which in the condensed phase occur on time scales of tens of femtoseconds for vibronic transitions, and in the femto- to picosecond time domain for vibrational excitations.

In the density matrix formalism, the polarization is given by the expectation value of the dipole moment $\mu$:

$$P(t) = \mathrm{Tr}\left[\mu\rho(t)\right] \equiv \langle \mu\rho(t) \rangle \tag{3.5}$$

where the term $\langle \mu\rho(t) \rangle$ denotes averaging over the ensemble described by the density matrix. For a given level system, it is usually calculated using perturbation theory. Diagrammatic methods, specially double-sided Feynman diagrams, have been used [76] to keep track of the various terms of perturbation theory, exploiting methods

that simplify the calculation, such as time ordering rotating wave approximation (to neglect non resonant contributions), phase-matching (the geometry of the experimental setup allows to reduce the number of terms in the nonlinear response function). A detailed theory describing ultraviolet pump/mid-infrared probe experiments for several examples can be found in Ref.[77].

### 3.2.1 Free Induction Decay and Cross-Phase Modulation

As the temporal resolution is improved in the time-resolved vibrational and electronic spectroscopies it becomes increasingly important to take into account the influence of the pulse characteristic for the analysis of the spectra. The accessible time resolution in femtosecond infrared experiments is shorter than the typical phase relaxation time of a vibronic transition. Therefore, coherent interaction of the light pulses with the sample may disturb the observed absorbance signals. Coherence produces an artifact known as *Perturbed Free Induction Decay (PFID)*, which may be misinterpreted as an intrinsic incoherent temporal evolution of the sample [78]. The interaction of the visible field with an electronic transition, and the IR field with a vibrational transition is quite different in condensed phase as compared with gas phase systems, infact, the line widths of electronic transitions of molecules in solution, typically range from a few hundreds wavenumbers to thousands of wavenumbers. In the case of homogeneous broadening, the full width half maximum ($\Delta\upsilon FWHM$) of the absorption line is related to the dephasing time, $T_2$ by:

$$T_2 = \frac{1}{\pi \Delta\upsilon FWHM} \tag{3.6}$$

Although electronic transitions may have a significant inhomogeneous broadening component, it can still be deduced that the characteristic time for dephasing of electronic transitions is in the order

of 10 to 100 fs. Vibrational line widths, in contrast, are rarely larger than 50 $cm^{-1}$ and values in the range 525 $cm^{-1}$ are common. More frequently, vibrational transitions in non-associated solvents are expected to dephase exponentially with a phase relaxation time on the order of 500-1000 fs, a time scale that is definitely longer than the achievable pulse duration of the IR probe pulses, which are in the order of ∼100 fs. In UV-Vis pump/mid-IR probe experiments, an intense pump pulse is used to trigger a photoreaction by electronic excitation. The response of the sample is probed by monitoring, as a function of the delay time $\tau$ between pump and probe, the absorbance change of the sample by means of a weaker probing pulse. Therefore, an absorbance change due to real kinetic components is expected only at positive delay times. However, due to the long dephasing time of ground-state vibrational transitions, the IR-probing pulse may resonantly create a vibrational coherence (coherent polarization), which decays with its intrinsic dephasing time $T_2$. This coherent polarization acts as a source of radiation (the so-called free-induction decay), and the IR-detector will record both the probing pulse and the radiated polarization. If an excitation pulse reaches the sample after the probing pulse (at negative delay times), it can not influence the intensity of the probing pulse itself. However, it may influence the temporal or spectral properties of the probe-induced free-induction decay signal of the sample, whenever the electronic excitation process modifies the strength or position of the ground-state absorption line. As a consequence, in the case of frequency resolved detection, the IR-detector will record a difference signal which decays toward negative delay times with an intrinsic time constant $T_2$. The perturbed free-induction decay signal is a consequence of dephasing and essentially reflects the spectral properties of the sample in the ground state and in the excited states. It does not reflect any temporal evolution of the sample related to a photoinduced process. The evidence

of absorbance changes at negative delay times is not, in any way, a violation of the causality principle, it is rather the consequence of the fact that pump and probe spectroscopy is a third order nonlinear experiment, where both transient polarization and population dynamics contribute to the measured signals. Therefore, a realistic description of the molecular dynamics requires to distinguish between contributions of the difference signal caused by these coherent effects and the real kinetic components, reflecting population dynamics. The description of the perturbed free-induction decay can be done as follows[79]. Let us consider the interaction between a single homogeneously broadened IR-absorption line and a resonant femtosecond IR-probing pulse. The probing IR pulse $E_i(t)$ generates a coherent polarization in the sample which subsequently decays with its intrinsic dephasing time $T_2$. The field radiated by this coherent polarization propagates in the same direction as the probing pulse, and therefore is measured by the detector. Solving the Bloch equations in the low excitation limit (first order in $E_i(t)$), leads to writing the radiated field $E_r(t)$(the so-called free-induction decay) as:

$$E_r(t) = \int_{-\infty}^{+\infty} M(t-t')E_i(t')dt' \tag{3.7}$$

where M(t) is the medium response to impulsive excitation (i.e. to a $\delta$-shaped pulse) Eq.3.3 can be expressed in the frequency domain as:

$$E_r(\omega) = M(\omega)E_i(\omega) \tag{3.8}$$

In a pump probe experiment with frequency solved detection, the collected intensity is given by:

$$I(\omega) = |E_i(\omega)+E_r(\ddot{I})|^2 = E_i(\omega)|^2+|E_r(\omega)|^2+2ReE_i(\omega)E_r(\omega) \tag{3.9}$$

Assuming weak absorption, $|E_r(\omega)|^2$ is negligible with respect to the other terms. An interaction between an excitation pulse and an incoming IR-probing pulse $E_i$(t) is impossible when the excitation pulse reaches the sample after the IR-probing pulse (i.e. at negative delay times). However, the excitation pulse may interact with the free-induction decay light field $E$r(t). In what follows $\mathrm{E}_r(\omega)$ and I($\omega$) denote the field and intensity of the unperturbed sample (in absence of the excitation pulse), and $\mathrm{E}_r$, $\omega$(t) and $\mathrm{E}_\tau(\omega)$ the light field and intensity radiated by a polarization that has been perturbed by a pump pulse delayed by $\tau$ with respect to the probe pulse. In this case the difference in the transmitted intensities with and without pump is given by:

$$\Delta I_\tau(\omega) = I_\tau(\omega) - I(\omega) = 2ReE_i^*[E_{r,\tau}(\omega)E_r(\omega)] \tag{3.10}$$

The equations 3.7, 3.8 and 3.10 do not depend on specific assumption for the broadening mechanism (homogeneous or inhomogeneous). Since the free-induction decay is a linear effect, they are valid for both cases and even in the case of overlapping absorption bands, provided that a suitable response function M(t) is used, related to the shape of the absorption spectrum. For a Lorentzian shaped absorption line (homogeneously broadened with a dephasing time $\mathrm{T}_2$), M(t) can be written as:

$$M(t) = \Theta(t)e^{\frac{-t}{T_2}}e^{-i\omega_a t} \tag{3.11}$$

where $\Theta$(t) is the Heaviside function and $\omega_a$ is the center frequency of the absorption line. In this case, M($\omega$) is a Lorentzian function with center frequency $\omega_a$. It is convenient to introduce the function G$\tau$(t), which describes the relative variation of the pump-induced polarization (i.e. the change in the oscillator strength of the IR absorption line upon electronic excitation):

$$G(t) = \frac{E_r(t) - E_{r,\tau}(t)}{E_r(t)} \tag{3.12}$$

With this notation, the difference signal has the following general expression:

$$\Delta T(\omega,\tau) = \frac{\Delta I_\tau(\omega)}{I_i(\omega)} = \tag{3.13}$$
$$= \frac{-2ReE_i^*(\omega)\int_{-\infty}^{+\infty} G_\tau(\omega')M(\omega-\omega')E_i(\omega-\omega')d(\omega)}{E_i^*(\omega)E_i(\omega)}$$

Considering the situation where the excitation pulse leads to a bleaching of the IR absorption line: the radiated field $E_r(t)$ disappears when the excitation pulse reaches the sample. In the simplified case of $\delta$-shaped excitation and probing pulses, we have $G_\tau(t) = \Theta(t+\tau)$ and $E_i\omega = 1$, and assuming homogeneous broadening, is possible to solve Eq. 3.9 analytically:

$$\Delta T(\omega,t) \begin{cases} -e^{\frac{\tau}{T_2}} \frac{cos[(\omega-\omega_a)\tau]+(\omega-\omega_a)\sin[(\omega-\omega_a)\tau]}{(\omega-\omega_a)^2+\left(\frac{1}{T_2}\right)^2} & \tau < 0 \\ -\frac{1}{(\omega-\omega_a)^2+\left(\frac{1}{T_2}\right)^2} & \tau > 0 \end{cases} \tag{3.14}$$

For positive delay times the signal does not evolve with time and shows a Lorentzian band shape. At negative delay times, the typical features of the perturbed free-induction decay appear: at the center of the absorption line, the signal shows oscillations as a function of time, with a frequency equal to the detuning between line center and detection frequency $(\omega - \omega_a)$. In the case of infinite time resolution, perturbed free-induction decay is observed strictly at negative delay times, and all processes are separated in time, as a consequence of the temporal asymmetry of the light field originating from the free-induction decay: perturbed free-induction decay ($\tau < 0$), excitation

($\tau$= 0) and reaction or relaxation dynamics ($\tau > 0$). In an experiment with realistic time resolution, a mixture of all this processes takes place within the cross correlation time of the pump and probe pulses. Thus, the observation of fast molecular reactions is strongly hindered by perturbed free-induction decay. Another artifact to be taken into account performing UV-Vis pump/mid-IR probe experiments which derives from the non-linear response of the solvent and of the sample cell itself is the *Cross Phase Modulation (XPM)*. This phenomenum is observed when a strong pump pulse modulates the refraction index seen by the probe. This effect is enhanced when the probe pulse is chirped and causes the distortion of the transient signal in both the frequency and the time domains. In our group a detailed simulation of XPM in the mid-infrared region and in close conditions to the experimental ones has been done [80]. Our simulation takes into account the different group velocities of the pump and probe pulses and includes the influence of the linear chirp of the mid-infrared pulse and its asymmetry. The results of our numerical calculations fit very well the experimental signals measured in a 2 mm thick $CaF_2$ window. When an ultrashort pulse propagates through a medium, it distorts the electronic distribution of atoms and molecules and as a consequence modify temporarily the refractive index seen by the pulse itself [81]. This process induces a time modulation of the pulse phase and generates new frequencies. The pulse phase modulation can be generated by the pulse itself and the phenomenon is defined self-phase modulation (SPM). It can be also generated by a copropagating pulse and cross-phase modulation (XPM) is observed. In experiments with middle infrared (mid-IR) probe pulses the sample thickness is a fraction of that of the windows and the length of the spatial overlap between pump and probe is greater than that. Therefore signals originates mainly from the cell windows rather than from the sample contained within them. XPM, as any other off resonance signals,

produced during the temporal overlap of the two pulses, may have an intensity comparable or even stronger than the signal itself, thus seriously modifying the spectral and temporal profiles of the signal to be measured. If one needs to analyze in the first picosecond the spectral evolution due to the sample itself, it is necessary to evaluate the contribution of SPM and XPM. The total energy of the probe remains constant during the propagation but it is distributed on different frequencies. The probe spectrum is broadened and the pulse envelope develops an oscillatory structure. It's possible to utilize a simplified model where SPM can be neglected because the probe pulse is less intense than the pump. The propagation of an optical wave through a non-linear medium is described by the wave equation, that is a scalar equation if both pulses are linearly polarized[75, 82, 83]:

$$\nabla^2 E' - \frac{1}{c^2}\frac{\partial^2}{\partial t^2}(n^2 E') = 0 \tag{3.15}$$

where $E'$ is the total electric field and $c$ is the light velocity in vacuum. The refractive index, as function of the frequency, presents a linear part $n_0$ and a non-linear part that depends on the intensity of the total electric field impinging on the sample[75, 82]:

$$n(\omega) = n_0(\omega) + n_2 I \tag{3.16}$$

where $n_2 = 3\chi^{(3)}/8n_0$ is the non-linear refractive index [**?**]. The frequency dependence of the linear part of the refractive index is responsible for the group velocity dispersion (GVD). If we represent the electric field of a pulse as:

$$E(x,y,z,t) = R\left(F(x,y)A(z,t)e^{i(\omega t - kz)}\right) \tag{3.17}$$

we can define the group velocity as:

$$\upsilon_g = \left[\frac{dk}{dw}\right]^{-1} \tag{3.18}$$

and the GVD coefficient as:

$$\beta^{(2)} = \frac{d^2k}{dw^2} \tag{3.19}$$

The GVD effect comes out from the frequency dependence of the linear part of the refractive index. The non-linear effects are included through the parameter $n_2$ that, in general, can be considered as a constant in respect to the frequency. The intensity is the squared module of the total electric field $I = |E|^2$, where the total electric field is:

$$E'(x,y,z,t) = R(F_{pu}(x,y)A_{pu}(z,t) \times exp[i(k_{pu}z - \omega_{pu}t)] +$$

$$F_{pur}(x,y)A_{pr}(z,t) \times exp[i(k_{pr}z - \omega_{pr}t)]) \tag{3.20}$$

where $\omega_{pu}$ and $\omega_{pr}$ are the optical frequency of the pump and probe pulses, $k_{pu} = n_{pu}\omega_{pu}/c$ and $k_{pr} = n_{pr}\omega_{pr}/c$ are the wave vectors, and $n_{pu} = n(\omega_{pu})$ and $n_{pr} = n(\omega_{pr})$ the linear refractive index at the carrier frequencies. $F_{pu}(x,y)$ and $F_{pr}(x,y)$ describe the transverse distributions of the two fields; they play a role in calculating the overlap integral. This transverse distributions are in general different for two pulses because of the difference in the center wavelengths, nevertheless the differences among various overlap integrals are small and an effective cross sectional area $A_{eff}$ is introduced [82]. At this point, we can substitute the expression of the total field into the wave equation. In order to make life simpler it is possible also to apply the slowly-varying-envelop approximation, and expand $k_j$ in a Taylor

series around the respective central frequencies up to the second order. In this contest, the derivation of the coupled-amplitude equation is easy:

$$\frac{\partial}{\partial z}A_{pu}(z,t) + \frac{1}{v_{gpu}}\frac{\partial}{\partial t}A_{pu}(z,t) + \frac{i}{2}\beta_{pu}^{(2)}\frac{\partial^2}{\partial t^2}A_{pu}(z,t) =$$

$$i\gamma_{pu}\left(|A_{pu}(z,t)|^2 + 2|A_{pr}(z,t)|^2\right)A_{pu}(z,t)$$

$$\frac{\partial}{\partial z}A_{pr}(z,t) + \frac{1}{v_{gpr}}\frac{\partial}{\partial t}A_{pr}(z,t) + \frac{i}{2}\beta_{pr}^{(2)}\frac{\partial^2}{\partial t^2}A_{pr}(z,t) =$$

$$i\gamma_{pr}\left(|A_{pr}(z,t)|^2 + 2|A_{pu}(z,t)|^2\right)A_{pr}(z,t) \qquad (3.21)$$

where the nonlinearity coefficients $\gamma_j = \frac{n_2\omega_j}{cA_{eff}}$ are introduced. The first terms in the right-hand side of the equations represents, respectively, the SPM of the pump and of the probe, while the second terms are, respectively, the XPM induced into the pump by the probe and vice versa. In the case of a pump-probe configuration, it is possible to reduce the equations making some approximations:

- when weak probe pulses are used, their SPM contribution can be neglected, as well as the XPM induced into the pump by the probe.
- the sample thickness (a 2 mm thick $CaF_2$ window) is short in respect to the dispersion length, this mean that the GVD effects are negligible, $\beta_{pu}^{(2)} = \beta_{pr}^{(2)} = 0$

The equations are then reduced:

$$\frac{\partial}{\partial z}A_{pu}(z,t) + \frac{1}{v_{gpu}}\frac{\partial}{\partial t}A_{pu}(z,t) = i\gamma_{pu}|A_{pu}(z,t)|^2A_{pu}(z,t)$$

$$\frac{\partial}{\partial z}A_{pr}(z,t) + \frac{1}{v_{gpr}}\frac{\partial}{\partial t}A_{pr}(z,t) = i2\gamma_{pr}|A_{pu}(z,t)|^2A_{pr}(z,t) \qquad (3.22)$$

It is convenient to evaluate the solutions of equations 3.22 in a new coordinate system $(z, \tau)$ moving with the group velocity of the probe pulse and normalized to its time duration $\tau_{pr}$[82]:

$$\tau = \frac{t}{\tau_{pr}} - \frac{1}{\tau_{pr}} \frac{z}{\upsilon_{gpr}} \tag{3.23}$$

In this reference frame the coupled amplitude equations take the following form:

$$\begin{aligned} \frac{\partial}{\partial z} A_{pu}(z,\tau) &= i\gamma_{pu} |A_{pu}(z,\tau)|^2 A_{pu}(z,\tau) \\ \frac{\partial}{\partial z} A_{pr}(z,\tau) + \frac{\epsilon}{L_W} \frac{\partial}{\partial t} A_{pr}(z,\tau) &= \\ &= i2\gamma_{pr} |A_{pu}(z,\tau)|^2 A_{pr}(z,\tau) \end{aligned} \tag{3.24}$$

where $\epsilon = sgn(\upsilon_{gpu} - \upsilon_{gpr})$ and $L_W = \frac{\tau_{pr}}{|\upsilon_{gpu}^{-1} - \upsilon_{gpu}^{-1}|}$ is the walk-off length. For such a system it is possible to calculate an analytical solution. XPM and group velocity mismatch are taken into account while higher order effect due to GVD broadening are not considered. The general solution evaluated at the end of the sample $z = L$ is:

$$\begin{aligned} A_{pu}(L,\tau) &= A_{pu}\left(0, \tau - \epsilon \frac{L}{L_W}\right) e^{i\phi_{pu}} \\ A_{pr}(L,\tau) &= A_{pu}(0,\tau) e^{i\phi_{pr}} \\ \phi_{pu}(\tau) &= \gamma_{pu} L |A_{pu}(0,\tau)|^2 \\ \phi_{pr}(\tau) &= 2\gamma_{pr} \int_0^L \left| A_{pu}\left(0, \tau - \epsilon \frac{z}{L_W}\right) \right|^2 \mathrm{d}z \end{aligned} \tag{3.25}$$

The XPM contribution changes along the sample because of the group velocity mismatch (GVM) and it is obtained by integrating along the sample length L. In order to perform the integration it is necessary to give a specific shape to the two pulses. These are the initial conditions. Simulations have been performed for different initial conditions. The pump pulse in all the cases is represented by an unchirped gaussian pulse delayed in time in respect to the probe pulse:

$$A_{pu}(\tau) = A_{0pu} e^{-\frac{4\log 2}{\tau_{pu}^2}(\tau+\Delta T)^2} \tag{3.26}$$

$\Delta T$ is the delay time between pump and probe. In the calculus two types of probe pulses have been considered: a chirped symmetric gaussian pulse and a chirped asymmetric pulse.

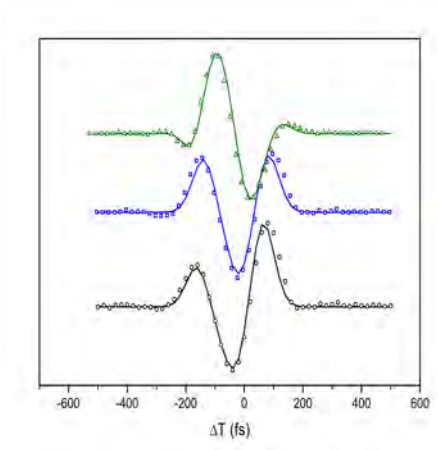


**Figure 3.1:** Simulation (line) done with an asymmetric chirped probe pulse. Chirp 1.8 * $10^{-4}$fs$^{-2}$, $\tau_{pr}$ = 120 fs. The open circles are the experimental curves taken at $\nu$ = 1608 cm$^{-1}$, the open squares are the experimental curves taken at $\nu$ = 1634 cm$^{-1}$ (at the band center frequency) and the open triangles are the experimental curves taken at $\nu$ = 1736 cm$^{-1}$[80].

In conclusion, as is shown in Fig.3.1, in order to reproduce the ex-

perimental XPM it is necessary to utilize asymmetric pulse envelopes with chirping. By adjusting these two parameters it is possible to perfectly fit the experimental time curves.

### 3.2.2 Experimental Set-Up

Our laser system is a standard kHz Ti:Sapphire amplified system, the Coherent Legend Elite. It is a compact Ti:Sapphire regenerative amplifier that delivers pulse energies over 3 mJ at 1 kHz repetition rate, with a pulsewidth $< 35$ fs and $M^2 < 1.35$. Legend Elite is a single-stage regenerative amplifier that uses thermo-electrically (TE) cooled Ti:S crystal. For seeding the Legend-Elite, the oscillator is a Coherent Micra, which delivers broad bandwidth (>100 nm) mode-locked pulses with high average power (300 mW) from an integrated Verdi-5 W pump laser. To optimize the seeding of any ultrafast amplifier, the Micra presents an adjustable spectral bandwidth (from $< 30$ nm to over 100 nm) and center wavelength tunability. Femtosecond laser pulses are commonly generated in the solid state material Titanium-Sapphire (Ti:Sapphire) and operate in the near-infrared region around 800 nm. However, for many experiments other wavelengths towards the ultraviolet, visible or mid-infrared are required for exciting and probing the molecular system under study. In Pump-Probe experiments very short pulses and tunability of both pump and probe pulses are necessary. Therefore an ideal system for pump-probe spectroscopy should provide pulses that are as short as possible, broadly tunable and the frequencies of pump and probe pulses should be independently selectable. When intense light interacts with nonlinear materials, non linear optical phenomena appear[84]. These effects can be exploited to generate new frequencies, and thus to extend the spectrum of known laser frequencies to the desired mid-IR and UV-Vis range. The basis process is a second order nonlinear optical process and require solid state materials with a nonvanishing second order nonlinearity

($\chi^{(2)}$). In practice when two waves at frequencies $\omega_1$ and $\omega_2$ propagate through a nonlinear crystal, a third wave at frequency $\omega_3$ is generated by the $\chi^{(2)}$ process. This process is called Sum Frequency Generation (SFG) when the generated frequency is $\omega_3 = \omega_1 + \omega_2$. When $\omega_1 = \omega_2$ we have Second Harmonic Generation (SHG). In Difference Frequency Generation (DFG), pulses at $\omega_1 = \omega_3 - \omega_2$ are generated from two input pulses at $\omega_3$ and $\omega_2$. Another important nonlinear interaction is Optical Parametric Generation (OPG). In this process, a pump pulse at frequency $\omega_3$ generates, in a nonlinear crystal, two new pulses at $\omega_1$ and $\omega_2$ (*idler* and *signal*), starting from quantum noise. If in addition, a weak seed pulse at frequency $\omega_1$ or $\omega_2$ is present together with the pump, there will be an amplification of the signal or idler, which constitutes the Optical Parametric Amplification (OPA). The efficiency of the parametric generation depends on the relative phase an direction of the interacting pulses, which is the *phase matching condition*. The phase matching can be realized either collinearly (scalar phase matching), or non collinearly (vector phase matching). In the collinear case, the phase matching condition is:

$$\mathbf{k_3} = \mathbf{k_1} + \mathbf{k_2} \tag{3.27}$$

or

$$\omega_3 n_3 = \omega_1 n_1 + \omega_2 n_2 \tag{3.28}$$

where $|\mathbf{k_1}| = n_1 \cdot \left(\frac{\omega_1}{c}\right)$. The $\chi^{(2)}$ processes can not happen in symmetric media. In birefringent crystals[85] this condition can be satisfied using different polarizations for the interacting pulses. The most commonly used crystal in OPG-OPA setups is the $\beta - BaB_2O_4$ (BBO). BBO crystal has a high damage threshold and supports large bandwidth, so it is a good candidate for parametric generation with intense femtosecond pulses. When it is pumped with the fundamental

Ti:sapphire wavelength, it is able to generate frequencies covering the range from 1 $\mu$m to 3 $\mu$m. the frequency tuning is achievable through the phase matching condition Eq. 3.28: the pair of signal and idler $\omega_1$ and $\omega_2$ can be tuned continuously changing indices $n_1$, $n_2$ and $n_3$, controlling the crystal orientation, the temperature, pressure or electric field applied to the crystal[86].

### 3.2.3 Femtosecond Mid-Infrared Pulses

Mid-infrared pulses are obtained in two steps. In the first step, by optical parametric amplification, the pulses from the laser are converted into near-infrared signal and idler pulses ($\lambda_s \approx 1.2\mu m$, $\lambda_i \approx 2.4\mu m$). In the second step, the mid-IR pulses are generated by difference frequency generation in a $AgGaS_2$ crystal. The home-made OPA in our laboratory (Fig. 3.2) works in two stages: pre-amplification and amplification of the signal and idler generated into a type II BBO crystal that is seeded by single filament white light. The seeding white light is generated by focusing a portion of the amplified 800 nm pulses into a sapphire plate [87]. The white light is then recombined with the 10 % of the pump pulse onto the BBO crystal. The two beams are spatially and temporally overlapped. The light generated in this first pre-amplification process contain both signal and idler.

For the second amplification step, the undesired idler and residual 800 nm components are removed with dichroic mirrors. The remaining signal beam is sent again onto the crystal and overlapped spatially and temporally with the intense pump beam coming from the laser. The signal and idler are continuously tunable in the wavelength range from 1.2 to 2.4 $\mu$m, adjusting the phase match angle. It is important to notice that the type II phase matching guarantees the perpendicularity of signal and idler polarizations, thus they are already correctly aligned for the subsequent difference-frequency process. In the second step of the light conversion, signal and idler are separated by

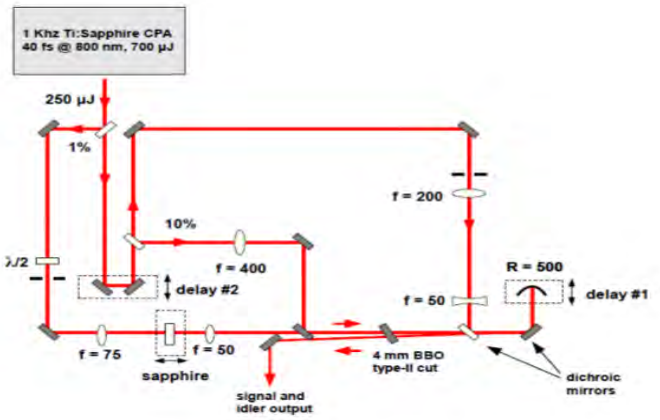


**Figure 3.2:** Two stages OPA for the generation of tunable femtosecond and idler pulses.

dichroic mirrors and recombined into a $AgGaS_2$ crystal [88]. The mid-IR pulses are obtained by difference-frequency generation of signal and idler. The pulses are tunable in a wide spectral range from 3 to $\sim 10$ $\mu$m [89]. The energy achieved from a mid-IR pulse is around $1-2\mu$J, with a time duration of $100-200$ fs and bandwidth of 200 $\text{cm}^{-1}$.

### 3.2.4 Femtosecond UV-Vis Pulses

Electronic excitation have been performed using either UV femtosecond pulses at 400 nm and Vis femtosecond pulses at 550 nm. The UV excitation pulses have been generated by Second Harmonic Generation (SHG) of a small fraction of the fundamental 800 nm pulses from the commercial Ti:Sapphire oscillator and regenerative amplifier in a type I $\beta - BaB_2O_4$ (BBO) crystal, cut under 29.1° with 100 $\mu$m thickness. The pump beam passes through a half-wave plate controlling the polarization and through a telescope in order to reduce

the beam diameter, thus the adjustment of the beam diameter at the sample position is facilitated. The visible excitation pulses, instead, have been generated by Sum Frequency Generation (SFG) of the idler output of a commercial optical parametric generator (TOPAS, Light Conversion) with a portion of the fundamental output at 800 nm in a type I BBO crystal. The pump beam polarization was set to magic angle with respect to the probe beam by rotating a half-wave plate. Anisotropy measurements were performed, istead, setting the pump beam polarization either at 0 or 90 degrees with respect to the probe beam.

### 3.2.5 Pump-Probe Set-Up

The setup scheme used for the experiments is reported in Fig. 3.3. The intense ultrashort IR pulse from the OPA is split into pump and probe beams, by means of a beam splitter. The mid-IR pump pulse, which is not used in the UV-Vis pump/mid-IR probe experiment, is then blocked. The recollimated probe pulse pass through a $BaF_2$ wedged plate which splits off two weak reflections used as probe and reference beams.

The 400 nm and the 550 nm pump pulses passes through a computer controlled delay line and is sent onto the sample together with the probe beam. The signal and reference beams are focused by a 30°off-axis parabolic mirrors into the sample, where pump and probe are spatially overlapped, whereas the reference beam crosses an area of the sample not perturbed by the pump. After the sample, the light is collimated and the pump beam is blocked. Finally, the probe and the reference are spectrally dispersed in a grating spectrometer and complete spectra are recorded simultaneously for each shot using a liquid nitrogen cooled double array ($2 \times 32$ pixels) of MCT detector. The sample is maintained between two $CaF_2$ windows, separated by a spacer whose thickness is chosen depending on the absorbance of the

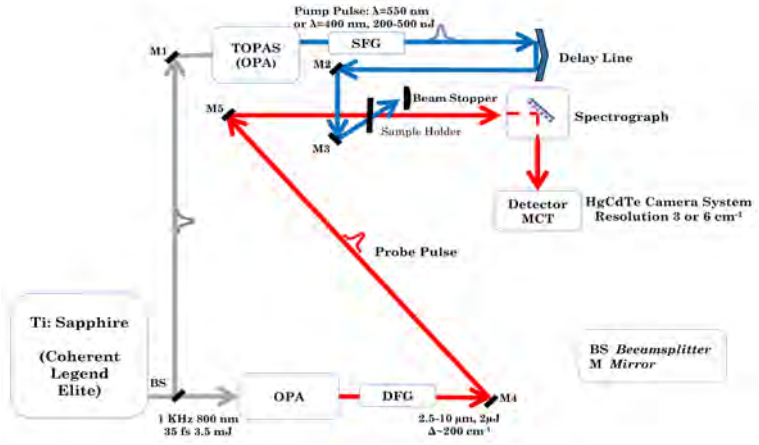


**Figure 3.3:** Experimental pump/probe setup.

sample. The two windows are mounted on a holder whose position can be varied with three manual linear stages, in order to position the sample in the focus of the crossed beams. The pump pulse is chopped at a frequency that is half of the repetition rate of the laser (500 Hz), in order to eliminate long term drifts effects, allowing a comparison of the probe intensity with and without pump pulse on two subsequent shots. In this way, it is easy to measure the transient absorption signal normalizing the change of absorbance with respect to the transmission of the reference pulses, and comparing on two subsequent shots with the unexcited case:

$$\Delta A = \log\left[\left(\frac{I_{\text{probe}}}{I_{\text{reference}}}\right)_{\text{pump on}}\left(\frac{I_{\text{reference}}}{I_{\text{probe}}}\right)_{\text{pump off}}\right]\cdot 1000 \quad (3.29)$$

To avoid spectral and temporal distortion of the mid-IR laser pulses due to the absorption of water vapor and $CO_2$, the whole pump/probe setup is purged with nitrogen gas. Significant pulse distortion of the infrared pulses is expected at frequencies where gaseous

components of air have resonant transitions (3700 $cm^{-1}$: stretching modes of $H_2O$; 1600 $cm^{-1}$: bending mode of $H_2O$; 2300 $cm^{-1}$: stretching mode of $CO_2$). In standard atmospheric air, propagation on distances of the order on several tens of cm produces dramatically distorted pulses, with long trailing wings due to the resonant interaction [90]. For reference purposes, the sample is replaced by a polished semiconductor (gallium arsenide: $GaAs$) window to determine the zero delay point and to control the pulse duration. The last part of the setup is constituted by the detection system. Essentially, the beams are first dispersed into a spectrometer and then the light is sent onto a double linear array of 32 sensors of mercury cadmium telluride (HgCdTe, MCT). The spectrometer used in the experiments is a TRIAX 180 from Jobin Yvon. It has three gratings mounted on a turret with three different blaze wavelengths and different spectral resolution. All moving parts of the TRIAX are automated. In particular, it is possible to control remotely by computer the grating selection, the working wavelength and the entrance slit width. Selecting different gratings, it is possible to vary the spectral window and the spectral resolution. Knowing the optical design of the double array detector and evaluating the dispersion of the spectrometer, it is possible to determine the spectral range and the spectral resolution provided by each grating. The front-end interface circuit for the MCT detector has been designed and developed completely at Lens. The MCT detector is made of 2 arrays of 32 sensors, this means that there are 64 signals to be measured. Each sensor has independent output and all the 64 channels have independent preamplifiers, gated integrators and sample-and-holds circuit. The peculiarity of this system is the introduction of a 32 to 1 multiplexer associated to for each array. The great advantage in using 2 multiplexer is that we have two serial output, each made up of 32 single signals. In this way the acquisition of the probe and reference signals, revealed by the two arrays,

results more convenient. In addition, the hardware architecture provides digital logic circuit, necessary to synchronize sampling on the external trigger coming from the laser. The MCT is triggered by the laser trigger at 1KHz. The two serial output from the front-end are sent to a computer for data acquisition. This task is exploited by a ADC card directly connected to the PC through a PCI bus. For our purpose, a sampling rate of 100kHz is enough. The board (PCI-DAS6013) provides up to 16 analog inputs, but we use just 3 of them, 2 for the signals from the front-end (probe and reference) and one for the chopper. The board is programmed in order to be externally triggered by the laser trigger. This guarantees that the acquisition is synchronized with the laser pulse and the signals reproduce the real spectrum. The acquisition program was developed in LabVIEW programming language by Dr. M. Lima. LabVIEW (Laboratory Virtual Instrumentation Engineering Workbench from National Instruments).

### 3.2.6 Experimental Details

*Bacillus subtilis* and *Thermobifida fusca* hemoglobins were obtained and purified as described previously (*Tf*-trHb was successfully obtained as a lyophilized sample) [51, 46]. Protein solution for Vis-pump Mid-IR-probe measurements were prepared by dissolving the samples in a TRIS-HCl buffer 0.2 M in $D_2O$ (pD=8). In case of *Tf*-trHb and Triple Mutant of *Tf*-trHb, 10-13 mM solutions were prepared by dissolving the lyophilized protein preparations in the buffer, while *Bs*-trHb solutions with a concentration of 4 mM were obtained by microcentrifugation with Millipore ultracon filters starting from a liquid preparation. Reduction of proteins was accomplished by adding a freshly prepared anaerobic solution of sodium dithionite in stoichiometric excess to the protein solution, previously degassed with nitrogen. Carbon monoxide (Rivoira), was gurgled at low flux intensity, and the sealed protein solution was saturated with 1 atm CO

for 15 minutes. In this way CO is homogeneously distributed in spite of the high viscosity of the sample. Samples for transient infrared measurements were prepared by squeezing about 40 $\mu$l of solution between two calcium fluoride windows (3 mm thickness) separated by a 50 $\mu$m teflon spacer (in case of *Bs*-trHb a 100 $\mu$m spacer was used). The OD at the excitation wavelength was about 0.8 for all samples. CO dissociation was induced by pumping the systems either with a 400 nm or a 550 nm laser pulses. In the case of UV excitation the pulses energy was ranged from 200 to 500 nJ, in the case of Vis excitation the pulses energy used was 200 nJ. The samples were moved with a home-built scanner to refresh the solutions and avoid photodegradation. Home-written software was used to collect the data over the two different spectral regions, respectively between 1880 and 1975 $cm^{-1}$ and from 2030 to 2230 $cm^{-1}$. The signals in every spectral region were recorded with freshly prepared samples and measured at least three times. To obtain a good signal-to-noise ratio in the case of the free CO signal, which has a small absorption cross section, a number of data sets, corresponding to about 12000 laser shots were collected and averaged. The integrity of the samples has been checked by FT-IR (Bruker Alpha-T) and visible absorption (Perkin-Elmer LAMBDA 950) spectra, collected before and after the time-resolved measurements.

### 3.2.7 Anisotropy Measurements

In order to determine the equilibrium orientation of carbon monoxide respect to the heme plane we performed time-resolved polarized mid-IR spectroscopy. Experiments were repeated by setting the pump pulse polarization either to 0 or 90 degrees with respect to the probe pulse, and the time dependent anisotropy of the transition was calculated assuming that the heme behaves like a circular absorber (the heme possesses a two-fold degenerate transition dipole in its plane)

when excited at 400 nm [91, 27]. When an isotropic sample solution is photolyzed or photoexcited with a linearly polarized pump pulse, those molecules whose transition dipole moments happen to be oriented along the polarization direction absorb light efficiently, thereby introducing an anisotropic distribution of photodissociated or photoexcited molecules in solution. Because of this anisotropic orientational distribution, the absorbance of the probe transition dipole of the sample will depend on whether the probe polarization is oriented parallel ($\Delta A^{\parallel}$) or perpendicular ($\Delta A^{\perp}$) to the pump polarization. The polarization anisotropy r(t) is defined as:

$$r(t) = \frac{\Delta A^{\parallel}(t) - \Delta A^{\perp}(t)}{\Delta A^{\parallel}(t) + 2\Delta A^{\perp}(t)} \tag{3.30}$$

and considering that photoyzing at 400 nm heme possesses a two-fold degenerate transition dipole in its plane r(t) is simply related to the orientation of CO according to:

$$r(t) = -0.3 \left\langle cos^2\theta(t) \right\rangle + 0.1 \tag{3.31}$$

Here the angle $\theta$ spans the range $0^\circ \leq \theta \leq 90^\circ$, giving rise to -0.2 $\leq$ r(t) $\leq$ 0.1.

Since rotational diffusion of the protein randomizes the orientation of the photoselected hemes, the polarization anisotropy at pump-probe delay time of zero, r(0), it is necessary to obtain the angles between transition dipoles, $\theta(0)$ free from the contribution of the orientational dynamics. If the measurement is made at a pump-probe time delay that is much shorter than the rotational diffusion time of the protein, the measured anisotropy can be approximated to r(0). Furthermore, since rotational diffusion for large molecule like a heme protein is well approximated by an exponential decay function, the r(0) is readily calculated from the measured anisotropy r(t).

### 3.2.8 Data Analysis

For the quantitative analysis of the time-resolved spectral data we used a combined approach, consisting of Singular Values Decomposition (SVD) and the simultaneous fitting of all the collected kinetic traces (global analysis). The SVD analysis has been widely used in many scientific fields [92]. SVD is a factorization procedure that reduces the data matrix to a series of orthogonal basis components. If $A(\lambda, t)$ is an $m$x$n$ matrix then the SVD returns three matrices, as below:

$$A(\lambda, \tau) = USV^T \tag{3.32}$$

where $U$ is an $m - by - m$ matrix, the matrix $S$ is $m - by - n$ with non negative numbers on the diagonal (as defined for a rectangular matrix) and zeros off the diagonal, and $V$ denotes an $n - by - n$ matrix. $U$ contains a set of orthonormal 'output' basis vectors, i.e. basis spectra as a function of $\lambda$. Associated with each basis is an eigenvalue in the diagonal matrix $S$, so that each diagonal element can be considered as a scalar 'gain' by which each corresponding input is multiplied to give a corresponding output. The orthonormal 'input' or 'analyzing' basis vectors are enclosed in matrix $V$ and the rows of the transpose $V^T$ express the time course of the spectra basis. The number of components that one have to consider is determined by the weight in the $S$ eigenvalue matrix. If the single value component, scaled according to its respective singular value, is comparable with the experimental noise, then the component will be neglected. In order to avoid the contribution due to perturbed free induction decay and cross-phase modulation [78, 83, 77, 93, 80] we have excluded from our analysis the spectra measured for delays shorter than 500 fs. We have extrapolated the number of components using SVD

[94, 95, 96] and then we have analyzed the whole ensemble of kinetic data by means of a global fitting procedure. The combination of global analysis and SVD is a very helpful analysis protocol, as it provides a good control on the number of components used to fit the data [95, 97, 98, 63, 99, 100]. The time constants resulting from the fitting of the right singular vectors were used as the starting point for the subsequent global analysis. The aim of global analysis is to decompose the two-way data matrix into time-independent spectra and wavelength-independent kinetics [99, 100, 101, 102]. Once the number of components has been identified, the second step involves the parametrization of the time evolution of the relative intensities of the spectral components. This was accomplished by assuming a first-order kinetics, describing the overall temporal evolution as the sum or combination of exponential functions. Global analysis was performed using the GLOTARAN package (http://glotaran.org) [100, 103, 104]. We have employed a linear unidirectional sequential model. The solution of the system of differential equations for the sequential model considering increasing lifetimes is:

$$c_l(t) = \sum_{j=l}^{l} b_{j,l} exp(-k_j t) \tag{3.33}$$

with:

$$b_{j,l} = \prod_{m=1}^{l-1} k_m / \prod_{n \neq j, n=l}^{l} (k_n - k_j) \tag{3.34}$$

$c_l$(t) represents the temporal evolution of the selected component, $k_j$ is the decay rate of the component j and the amplitudes $b_{j,l}$ of the exponential decays are defined for j≤l assuming $b_{11}$=1. The spectra associated to the various time constants are termed Evolution Associated Difference Spectra (EADS).

## 3.3 Steady State Spectroscopy

The absorption spectra have been recorded by a Lambda 950 Perkin Elmer model spectrophotometer. The FT-IR spectra have been recorded by a Bruker Optics $\alpha$-FT-IR spectrophotometer.

Chapter 4

# CO Rebinding in $TrHb_S$ : Results

In this chapter the results on carbon monoxide recombination dynamics in two wild type $trHb_s$ from *Bacillus subtilis* and *Thermobifida fusca* and in the mutant 3F-*Tf*-trHb studied with Visible-pump midIR-probe spectroscopy are reported. Moreover the band shapes of gaseous CO dissolved in solvents with different chemical-physical properties will be qualitatively compared with that of the free CO inside the distal pocket of the investigated proteins.

## 4.1 CO Vibrational Band Shape in Solution

The IR spectrum of gaseous CO Fig.4.1 (a) is characterized by a series of ro-vibrational lines constituting the branches P and R. This branches show a minimum absorption ($\nu_0$) located at 2143 $cm^{-1}$. This value corresponds to the central frequency. The J=0 $\rightarrow$ J=0 transition is not visible because of the selection rule $\Delta$J= $\pm$1 in the gas phase. When CO is dissolved in solvents or when it is in the liquid state one broad band with the maximum frequency $\nu_s$ is observed [105].

In the condensed phase spectra the individual ro-vibrational bands are obscured because the rotational energy levels are broadened by the collisions and by the splitting of the m degeneracy due to electric fields generated by neighboring molecules. We dissolved CO in a series of organic solvents with different properties in order to understand when possible the correletion between different chemical environments and the vibro-rotational spectrum of the molecule (the IR spectra are reported in Fig.4.1). In Tab.4.1 the chemical-physical properties of the solvents used in this analysis are reported.

Carbon monoxide dissolved in carbon tetrachloride Fig.4.1 (d) shows a band located at 2135 cm$^{-1}$, this means that the maximum is downshifted of 8 cm$^{-1}$ respect to the gas frequency $\nu_0$; next to the central band two wings remain distinguishable, which are superimposable to the envelopes of the P and R branches of the gas phase. When CO is dissolved in a more polar solvent like chloroform, as shown in Fig.4.1 (e), the two wings almost disappear and the maximum of the frequency is downshifted of $\approx$ 6 cm$^{-1}$ respect to the gas value. In CO dissolved in hexane a very broad band centered at about 2143 cm$^{-1}$ is observed (Fig.4.1 (f)); this band is merged with the contributions due to the P and R branches. In acetonitrile (Fig.4.1 (c)), the most polar solvent we have used, we found a band centered at a frequency $\nu_s$ of 2137 cm$^{-1}$ and the wings relative to the P and R branches are completely disappeared. Lastly we dissolved CO in benzene (Fig.4.1 (b)) and we found a band located at 2133 cm$^{-1}$ which conformation mantains the two lateral wings as observed for carbon tetrachloride; moreover the frequency shift respect to the gas value is $\approx$ 10 cm$^{-1}$ for this apolar solvent. It is possible to notice that the wings, observed on the sides of the bands centered at a frequency $\nu_s$, for CO dissolved in apolar solvents coincide with the envelope of the P and R branches of the gaseous CO infrared spectrum. The spectra of the solutions in which a strong solute-solvent interaction is present,

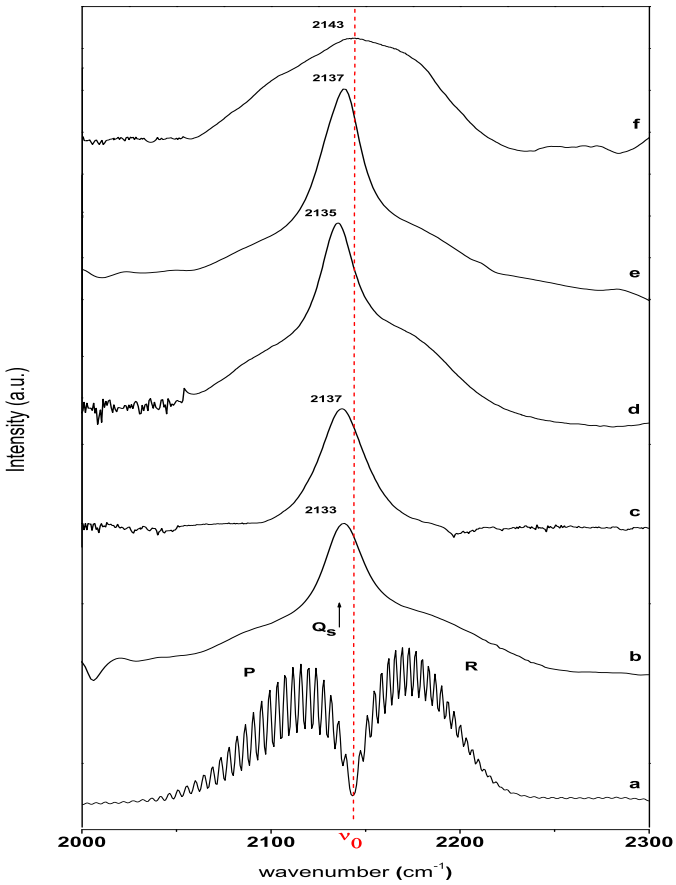


**Figure 4.1:** FT-IR spectra of gaseous CO (a) and CO dissolved in carbon tetrachloride(d), chloroform (e), hexane (f), acetonitrile (c) and benzene (b) obtained by flushing 1 ml solvent with 1 atm CO for 1 minute. The pathlength was 1 mm and the resolution was 0.9 $cm^{-1}$. $\nu_0$ indicates the central frequency of the gaseous CO absorption band (2143 $cm^{-1}$).

due to the solvent polarity and/or to solvents that provide molecular associations, show no shoulders independently from the position of the CO absorption band. The dissolved state leads to the formation of two kind of molecules: CO molecules which, preserving quasi-free

rotation, give rise to P and R branches and CO molecules in which the free rotation is frustrated by the action of the solvent and thus give rise to a more pronunced the central absorption ($Q_s$) branch located at the specific frequency $\nu_s$ depending on the nature (dielectric constant, dipole moment, polarizability, viscosity and density) of the solvent. The perturbation action of the solvent on the CO vibration produces branches $Q_s$ localized at a frequency lower than the frequency $\nu_0$ characteristic for the vibrator in the gaseous state. When CO has a strong interaction with the solvent, most of the molecules loses rotational freedom and only the $Q_s$ branch will be appreciable in the infrared spectrum, as in the case of CO dissolved in acetonitrile. The band center of of the liquid phase absorption is shifted in frequency from that of the gas phase absorption because of the perturbation of vibrational energy levels by the solvent and also by the dielectric constant of the medium [106]. The explanation is that the interaction with solvent causes a fraction of the molecules to undergo librational motion which appears with the fundamental vibration to produce absorption at the band center ($Q_s$ branch).

| Solvent | Dielectric Constant | Dipole Moment (D) | Polarizability ($C \cdot m^2 \cdot V^{-1}$) | Viscosity ($Pa \cdot s$) | Density ($g \cdot cm^{-3}$) |
|---|---|---|---|---|---|
| **Benzene** | 2.28 | 0.00 | 10.44 | 0.60 | 0.87 |
| **Acetonitrile** | 36.64 | 3.92 | 4.44 | 0.37 | 0.78 |
| **Carbon Tetrachloride** | 2.20 | 0.00 | 10.54 | 0.91 | 1.58 |
| **Chloroform** | 4.81 | 1.04 | 8.53 | 0.54 | 1.48 |
| **Hexane** | 1.88 | 0.00 | 11.45 | 0.30 | 0.65 |

**Table 4.1:** Chemical-physical properties of the solvent used in the analysis of CO IR bands [107].

As possible to notice from the values reported in Tab.4.1 and from the FT-IR spectra of Fig.4.1 there is not an univocal correlation between the bandwidth and the positions of the CO absorption band

and one single chemical-physical property of the particular solvent analyzed. Though the differences are quite small, however we can identify a trend in the change of the central frequency and of the band shape. We have compared the CO stretching band in three different apolar solvents: hexane, carbon tetrachloride and benzene. In these solvents is possible to observe the presence of P and R branches. The relative intensities of their central $Q_s$ band is correlated to the viscosity while its central position is somehow connect to specific interactions that give rise in benzene to a central band that is larger than in the other two solvents. The analysis of the CO stretching band in polar solvents (chloroform and acetonitrile) has shown that the complete disappearance of the P and R branches is observed only for acetonitrile; in chloroform the P and R branches are still appreciable but their intensities respect to the $Q_s$ band are small. We can draw the conclusion that viscosity and density regulate the bandwidth while the polarizability and the dielectric constant affect the position and the shape of the $Q_s$ band. It is important to underline the fact that in all the analyzed solvents the frequency shift compared to the gas value (2143 $cm^{-1}$) never exceeds 0.5%.

## 4.2 *Thermobifida fusca* trHb

### 4.2.1 Steady State Spectra

In Fig.4.2 and in Fig.4.3 the UV-Vis spectrum and the FT-IR spectrum of *Tf*-trHb-CO complex are reported.

As possible to notice from Fig.4.3 two bands corresponding to two different conformers of iron-bound CO are present. The lower frequency band, located at 1920 $cm^{-1}$ corresponds to the conformer in which CO is H-bonded to both TrpG8 and Tyr CD1, while the 1940 $cm^{-1}$ stretching band correspond to CO singly H-bonded to TrpG8. TrpG8 is the main residue stabilizing the coordinated CO. Otherwise,

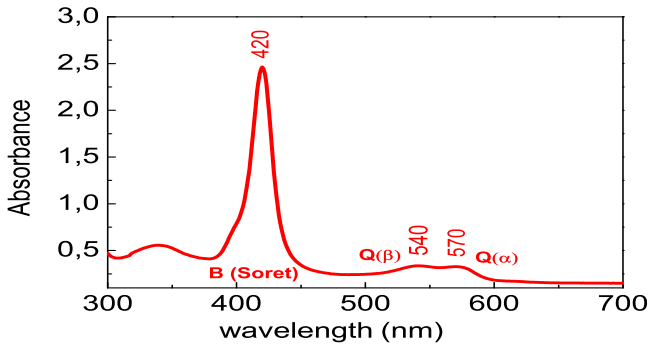


**Figure 4.2:** UV-Visible spectrum of *Tf*-trHb-CO complex. Protein solution was prepared by dissolving the lyophilized protein in a TRIS-HCl buffer 0.2 M in $D_2O$ (pD=8). The concentration of *Tf*-trHb was 10 mM , the cell pathlength 50 $\mu$m. CO was added after protein reduction with sodium dithionite (for more details see section 2.2.6).

TyrCD1 is very flexible and can interact with CO more weakly than TrpG8. This bonding network is responsible of an efficient stabilization of the exogenous ligand, but also of the dynamics of rebinding process and is due to the high polarity of the distal pocket residues (for more informations see section 1.2.1).

### 4.2.2 Time Resolved Mid-IR Spectra

In order to investigate the CO recombination dynamics in *Tf*-trHb-CO complex with UV-Vis pump mid-IR-probe spectroscopy we have triggered ligand dissociation either with 400 nm UV pump pulses or 550 nm visible pump pulses. In both cases we have monitored CO rebinding in two mid-IR regions: the region of the $\nu$(CO) stretching vibration of the iron-bound CO (1880-1990 cm$^{-1}$) and the dissociated free CO absorption region (2030-2230 cm$^{-1}$).

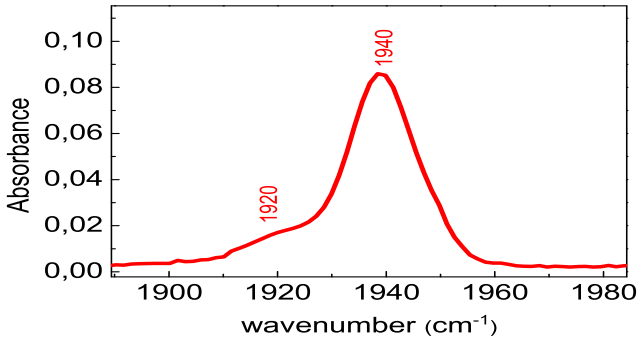


**Figure 4.3:** FT-IR spectrum of *Tf*-trHb-CO complex. Protein solution was prepared by dissolving the lyophilized protein in a TRIS-HCl buffer 0.2 M in $D_2O$ (pD=8). The concentration of *Tf*-trHb was 10 mM, the cell pathlength 50$\mu$m. CO was added after protein reduction with sodium dithionite (for more details see section 2.2.6).

### *Bound CO*

Initial experiments on *Tf*-trHb were performed by exciting the sample with a 400 nm pump pulse, whose energy was varied between 200 and 500 nJ (which corresponds to a power intensity ranging from 50 to 125 GW/cm$^2$). The spectrum recorded immediately after excitation shows the appearance of a bleaching signal in the spectral region where the ligated CO stretching vibration is expected, indicating photolysis of the ligand. A main bleaching band and a small shoulder are visible, respectively peaking at 1920 and 1940 cm$^{-1}$, in good correspondence with the absorption bands measured in the FT-IR spectrum of the CO adduct for this protein, see Fig.4.3 and Fig.4.4.

The analysis of the kinetic traces taken at the maxima of the two bleaching bands, reported in Fig.4.5, revealed a bi-phasic recovery, occurring within sub-nanosecond timescale. As clearly visible by inspection of the kinetic traces, the bleaching band at 1940 cm$^{-1}$ recovers

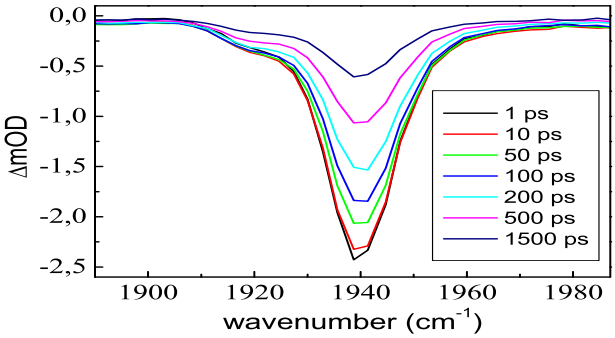


**Figure 4.4:** Time resolved spectra recorded at different time delays, showing the bleaching induced by the excitation at 400 nm in the $\nu$(CO) stretching region for the coordinated CO.

faster than the bleaching at 1920 cm$^{-1}$.

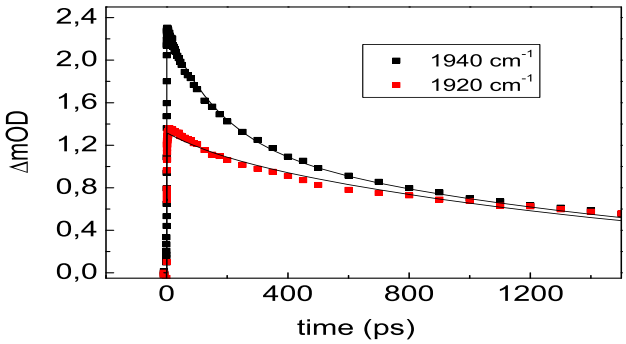


**Figure 4.5:** Kinetic traces (scattered points) at selected frequencies together with the fit (solid line) obtained by global analysis. The trace at 1920 cm$^{-1}$ has been scaled to overlap the trace at 1940 cm$^{-1}$ on the long time scale.

We have analyzed the data using a global fit (all wavelengths are fitted simultaneously) with a sequential decay scheme, obtaining the Evolution Associated Difference Spectra (EADS) reported in Fig.4.6.

The kinetic traces can be satisfactorily fitted with two components, whose time constants are 250 ps and 1.5 ns, respectively. The fast kinetic phase accounts for almost 40% of the recombination dynamics at 1940 $cm^{-1}$ (considering the error in the estimate of the nanosecond component). An inspection of the kinetic traces reported in Fig.4.5 brings out that the relative weight of the fast component is much higher for the 1940 $cm^{-1}$ band with respect to the low frequency band (1920 $cm^{-1}$).

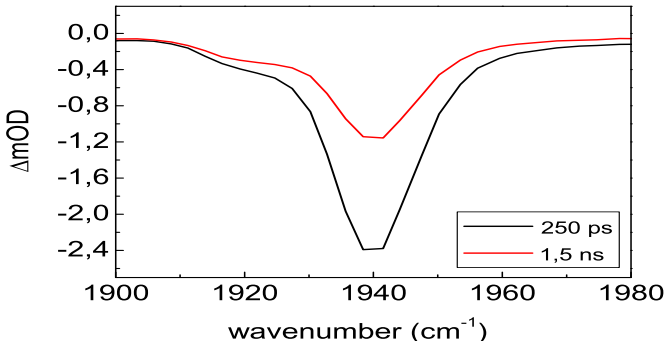


**Figure 4.6:** EADS (Evolution Associated Difference Spectra) obtained by globally analyzing all the kinetic traces recorded in the 1850-1950 $cm^{-1}$ spectral range after excitation at 400 nm.

Bleaching recovery on a sub-ns time scale can be directly associated to fast geminate recombination if it is assumed that the recombined CO and CO in the non-photolyzed portion of the sample have the same spectrum as the ligated CO at equilibrium [108]. In order to determine the equilibrium orientation of CO respect to the heme plane we performed time-resolved polarized mid-IR spectroscopy on *Tf*TrHb-CO complex. The pump pulses polarization was setted either to 0 or 90 degrees with respect to the probe pulse and the time dependent anisotropy of the transition was calculated as reported in section 2.2.7. We found that the time dependent anisotropy of the

transition results in an average value of -0.18 which mean that the coordinated CO is oriented in a way that the dipole forms an angle smaller than 15 degrees with respect to the heme normal, similarly to what observed for other globin proteins [108, 109, 30].

#### *Dissociated CO*

With the aim of further investigate the dynamics following CO photodissociation we also analyzed the free CO absorption band, which is expected to appear at about 2100-2150 cm$^{-1}$. Due to the low absorption cross section of the free CO vibration and to the substantial water absorption in that region, it is difficult to obtain reliable kinetic traces and time dependent spectra with a good signal-to-noise ratio. Tentative measurements, carried out by exciting the sample with a 400 nm pump pulse revealed a significant baseline problem, due to water absorption, heating, and excess energy dissipation in the system. In order to minimize these unwanted contributions, CO photolysis was triggered by exciting the heme in the Q-band absorption region (550-600 nm) instead of the B-band region. Under these experimental conditions the amount of energy dissipated by the system was significantly reduced. Measurements were thus carried out by setting the excitation pulse at 550 nm and probing both the $\nu(CO)$ stretching region for the coordinated CO and the free CO absorption region. The dynamic evolution in the bleaching region was substantially identical to what previously observed by exciting the sample at 400 nm. Instead, significant improvements were obtained in the free CO region, where time traces with good signal-to-noise ratio could be recorded.

Spectra in figure Fig.4.7 have been corrected for the presence of a baseline, which still contributes in this region although with a minor extent than in the previous measurements with 400 nm excitation. The baseline is removed by subtracting a third order polynomial fit.

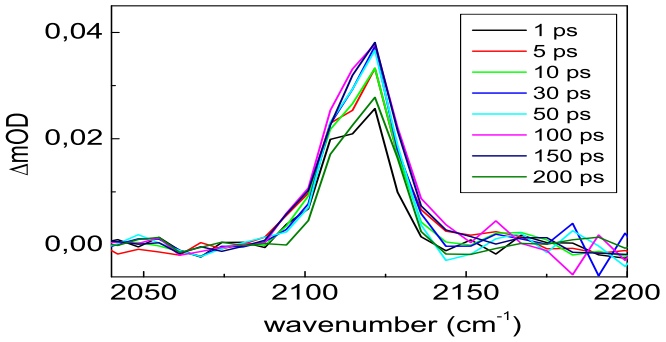


**Figure 4.7:** Time resolved spectra in the free CO region recorded at different time delays after excitation of the sample with a 550 nm laser pulse.

To remove the fluctuations of the baseline we applied the following procedure. The region between 2080 and 2150 $cm^{-1}$, where the signal is observed, was removed. A polynomial fit of the remaining signal was performed. Then, we subtracted the polynomial line to the entire signal achieving much cleaner spectra (see Fig.4.7). Our data show a ratio in the absorption cross section between the coordinated and docked CO of about 50, in agreement with previous findings [108]. Baseline problems are less significant in the bleaching region, which is free from water absorption. In this region, the amplitude of background fluctuation has a negligible influence on the signal. Fig.4.8 shows the kinetic trace measured at the absorption maximum and compared with that of the 1940 $cm^{-1}$ bleaching band, which has been scaled to match the intensity of the free CO signal. The two kinetic traces are well matched, except for the short time scale, where the signal corresponding to the free CO absorption (2120 $cm^{-1}$) shows an initial rise component.

These results confirm that also the fast 250 ps component has to be ascribed to geminate recombination. At the early measured times

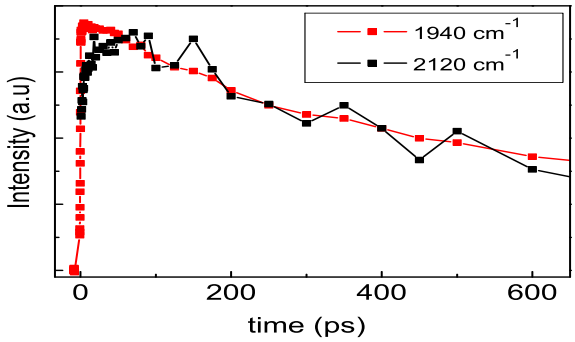


**Figure 4.8:** Kinetic traces at 2120 cm$^{-1}$ (black line), corresponding to the maximum absorption in the free CO region in *Tf*-trHb. The trace has been superimposed with the kinetic trace at 1940 cm$^{-1}$ (red line), corresponding to the maximum absorption of the coordinated CO.

a rise of the free CO absorption signal is observed, which can be fitted with a time constant of 30 ps. An initial rise component for a docked CO band has been previously observed also for myoglobin [30] and interpreted in terms of protein relaxation around the photolyzed CO molecule. In that case however the rise component had a much faster time constant of about 1.6 ps. Furthermore thermal relaxation has also been observed to occur for myoglobin excited at 597 nm, with a time constant of 6.2 ps [65]. The longer timescale observed in this case for the rise component may indicate a more significant protein rearrangement, possibly involving the rotation or reorientation of one or more amino acids side chains in the CO docking site. Such structural adjustment more likely modifies the electrostatic interactions around the CO molecule thus increasing the oscillator strength [110]. This is probably the consequence of a more flexible heme pocket structure, also brought out by the presence of a water molecule, which could rearrange by breaking/forming H-bonds with the tyrosine amino acids (TyrB10 and TyrCD1) located at short distance from the heme. The

measured CO absorption peak is quite asymmetrical and has a rather large bandwidth (FWHM $\approx$ 30 $cm^{-1}$), which suggests the presence of an inhomogeneous distribution of two unresolved bands behind the measured lineshape. The signal dynamically evolves by slightly shifting to the blue, but no substantial lineshape variations are observed. Although it has been shown that in similar systems a certain percentage (reported values span between 3.6 and 13%) of the photolized CO is initially in a vibrationally hot state [111, 109, 30, 32, 112, 113] no vibrational hot band could be resolved in the present case. Since the CO anharmonicity has been estimated to be 27-30 $cm^{-1}$ [111, 113] hot bands are probably not resolved due baseline fluctuation problems. Besides the 30 ps component, a global fit of the kinetic traces collected in the free CO region (2050-2200 $cm^{-1}$) results in two additional decay components, with time constants of 300 ps and 1.2 ns, respectively. These time constants substantially agree with those measured for the bleaching recovery, thus confirming that the process responsible for the dynamic evolution of the system is a fast geminate recombination of the photolized CO. In order to take into account of the bandwidth variation with time, we estimated the temporal evolution of the integrated area of the CO band, and we compared it with the kinetic trace at 2120 $cm^{-1}$, corresponding to band maximum. The two traces are in good agreement. These results do not completely agree with recent findings [45]. It has been found by transient absorption spectroscopy a geminate recombination with a time constant of $\approx$ 2 ns by exciting the *Tf*-trHb-CO complex with 400 nm femtosecond pump pulse. The fast ps component is observed only in infrared measurements. The reasons behind the observed discrepancies could be related to the different experimental conditions used in the two experiments. In the present case very high protein concentration (10 mM) is needed in order to obtain a measurable signal in the Mid-IR region; in transient absorption measurements, probing the UV-visible

range, sample concentration of 3.6 $\mu$M are instead utilized. Possibly the high concentration employed for infrared measurements gives rise to a very viscous sample or to the formation of aggregates, in which the CO rebinding kinetics could be altered. When considering the two other systems analyzed in this work, namely the truncated hemoglobin from *Bacillus subtilis* and the triple mutant from *Termobifida Fusca* (see sections 4.3 and 4.5) the outcome of visible transient absorption measurements and time resolved infrared measurements are in complete agreement. In fact, transient absorption measurements in the visible for 3F-*Tf*-trHb [114] led to the same results reported in this thesis. In light of the above considerations and on the basis of a structural analysis of the heme pockets of *Tf*-trHb and its triple mutant, it may be suggested that the conserved water molecule present in the pocket of *Thermobifida fusca* WT protein (see section 4.6) but not in that of the mutant protein plays an important role in determining the kinetics of CO rebinding. It is possible that at high concentrations this water molecule could be displaced or missing, causing a rearrangement of the pocket residues mostly interacting with the ligand, which could alter the rebinding kinetics of the WT protein. Such behavior is highlighted by the fact that in this protein the heme pocket is strongly exposed to the solvent being located in proximity of the protein surface.

## 4.3 *Bacillus subtilis* trHb

### 4.3.1 Steady State Spectra

The UV-Vis spectrum of *Bs*-TrHb-CO complex is very similar to that previous shown for *Tf*-trHb-CO complex and is reported in Fig. 4.9. Even in this case the iron bound CO is stabilized by hydrogen bonds. Two conformers can be observed (Fig. 4.10) one in which both TrpG8 and TyrB10 interact with bound CO (lower frequency stretching band

at 1888 $cm^{-1}$) and an other one in which only TyrB10 stabilizes the CO (higher frequency band located at 1925 $cm^{-1}$).

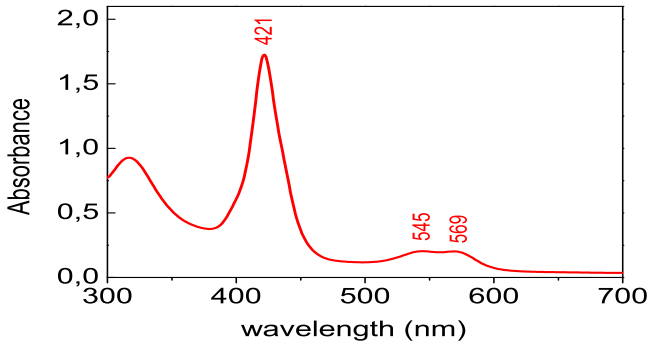


**Figure 4.9:** UV-Visible spectrum of *Bs*-trHb-CO complex. Protein solution was prepared by microcentrifugation with Millipore ultracon filters, the final concentration was 4 mM in TRIS-HCl buffer 0.2 M in $D_2O$ (pD=8), the cell pathlength 100$\mu$m. CO was added after protein reduction with sodium dithionite (for more details see section 2.2.6).

*Bs*-trHb heme pocket is characterized by four polar aminoacid TrpG8, TyrB10, GlnE11 and ThrE7 responsible of ligand stabilization through the formation of a hydrogen bonding network (see section 1.2.3).

### 4.3.2 Time Resolved Mid-IR Spectra

As for *Tf*-trHb both the absorption regions of the $\nu$(CO) stretching vibration of the iron-bound CO (1825-1975 $cm^{-1}$) and of the dissociated free CO absorption (2030-2230 $cm^{-1}$) were monitored.

#### *Bound CO*

Time resolved spectra in the bleaching region were collected by exciting the sample both with a 400 nm and a 550 nm laser pulse. Again, no

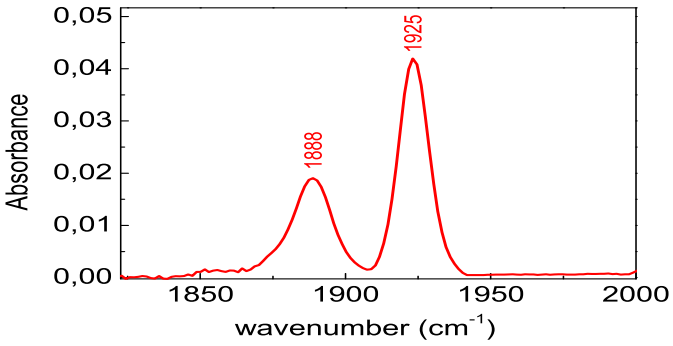


**Figure 4.10:** FT-IR spectrum of *Bs*-trHb-CO complex. Protein solution was prepared by microcentrifugation with Millipore ultracon filters, the final concentration was 4 mM in TRIS-HCl buffer 0.2 M in $D_2O$ (pD=8), the cell pathlength 100$\mu$m (for more details see section 2.2.6).

significant differences were observed in the dynamic evolution of the system between the two excitation wavelengths. Following CO photodissociation, two bleaching bands are observed at 1925 cm$^{-1}$ and 1888 cm$^{-1}$ respectively, whose positions well correspond with the measured FT-IR spectrum of the CO adduct for this protein (Fig.4.11).

The corresponding kinetic traces, reported in Fig.4.12 can be fitted with two time constants of 120 ps and 2 ns, respectively. In contrast to what observed in *Tf*-trHb, the two bleaching bands in *Bs*-trHb recover with the same kinetics. In this case the faster kinetic component has a very low weight, only accounting for less than 10% of the recombination dynamics for both the bleaching bands, implying that the fraction of picosecond geminate recombination is smaller than that observed in *Tf*-trHb. Fast geminate recombination in *Bs*-trHb has been previously observed through time resolved measurements in the visible spectral range [43]. In the present infrared measurements a 30 ps component, previously identified by transient absorption measurements in the visible region, is not observed. Since the currently

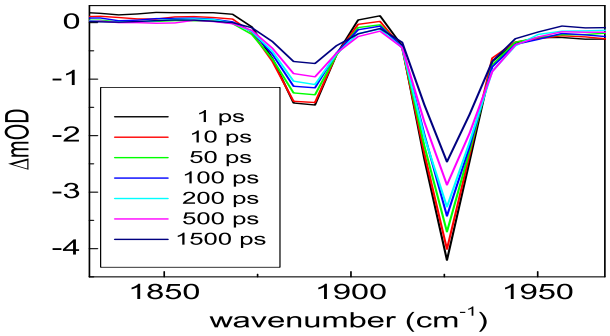


**Figure 4.11:** Time resolved spectra recorded at different time delays, showing the bleaching induced in *Bs*-trHb-CO complex in the $\nu$(CO) stretching region for the coordinated CO (excitation wavelength 550 nm).

probed spectral range is only sensitive to CO vibrations, we conclude that this 30 ps component is not associated to fast ligand recombination, but probably represents a relaxation process of the heme.

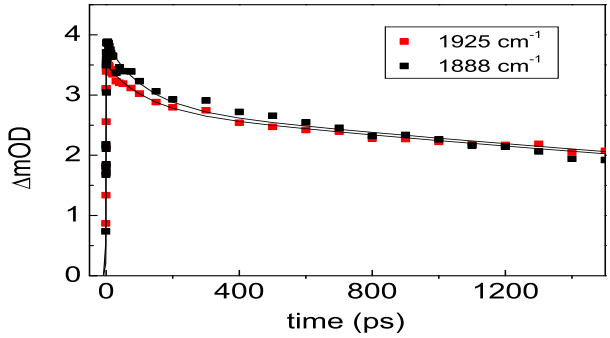


**Figure 4.12:** Kinetic traces (scattered points) together with the fit (solid lines) taken at the maxima of the two bleaching bands for *Bs*-trHb-CO complex. The trace at 1925 $cm^{-1}$ (red dots) overlaps the trace at 1888 $cm^{-1}$ (black dots).

### *Dissociated CO*

The free CO region was probed by exciting the sample at 550 nm. The time resolved spectra in this region are similar for *Bs*-trHb and *Tf*-trHb, but striking differences are observed in their kinetics. Also for *Bs*-trHb only one band is observed, whose dynamic evolution follows that of the bleaching signals, though with minor intensity. The peak shape of the docked CO is not completely symmetrical and the FWHM is about 30 cm$^{-1}$. Time resolved spectra of the free CO in *Bs*-trHb, shown Fig.4.13, show a blue shift on a 10 ps time scale, which could be an indication of vibrational cooling. Alternatively there could be two bands hidden under the observed lineshape, with a population exchange occurring on this timescale. Given the low signal to noise ratio of the measurements these observations have to be considered carefully, and in order to better rationalize this spectral evolution, measurements should be repeated with a higher spectral resolution.

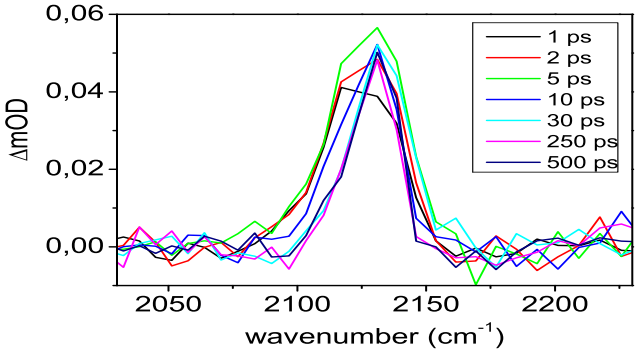


**Figure 4.13:** Time resolved spectra in the free CO region recorded at different time delays after excitation of the sample with a 550 nm laser pulse.

The kinetic trace recorded at the maximum of the absorption band, compared with that of the scaled bleaching trace measured at 1925 cm$^{-1}$ is reported in Fig.4.14. The two kinetic traces well overlap.

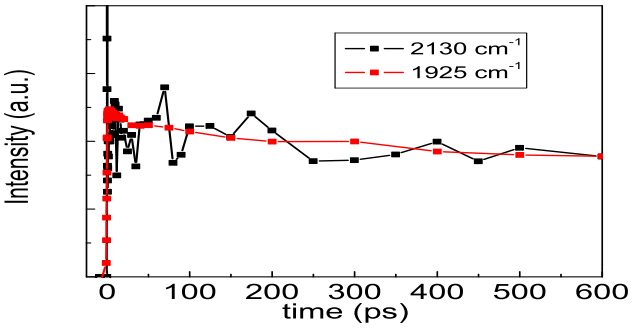


**Figure 4.14:** Kinetic traces at 2130 $cm^{-1}$ (black line), corresponding to the maximum absorption in the free CO region in *Bs*-trHb. The trace has been superimposed with the kinetic trace at 1925 $cm^{-1}$ (red line), corresponding to the maximum absorption of the coordinated CO.

## 4.4 Comparison Between *Tf*-trHb and *Bs*-trHb

In the first part of this study we have compared two $trHb_s$ from *Thermobifida fusca* and *Bacillus subtilis*. Despite the structural similarities in the architecture of the heme pocket, *Tf*-trHb and *Bs*-trHb display significant differences in the dynamics of ligand exchange and rebinding. Present results indicate that although both proteins show fast geminate recombination, the relative amount of the picosecond dynamic phase is not the same. In order to highlight these differences we have compared in Fig.4.15 and in Fig.4.16 the kinetic traces measured for the two bleaching bands of *Tf*-trHb (1940 and 1920 $cm^{-1}$) with the corresponding bands observed for *Bs*-trHb (1925 and 1988 $cm^{-1}$).

In Fig.4.17, the kinetic traces corresponding to the maximum absorption of the free CO band are compared. The observed signals bring out clearly a more intense slow phase and a faster decay in case of *Tf*-trHb with respect to *Bs*-trHb.

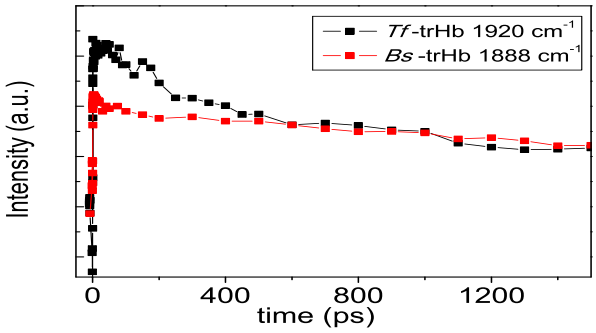


**Figure 4.15:** Comparison between the kinetic traces in the bleaching region for *Tf*-trHb and *Bs*-trHb upon excitation at 550 nm. Trace at 1920 cm$^{-1}$ of *Tf*-trHb (black line) is compared to the trace at 1888 cm$^{-1}$ of *Bs*-trHb (red line). The two kinetic traces have been scaled to overlap on the long time scale.

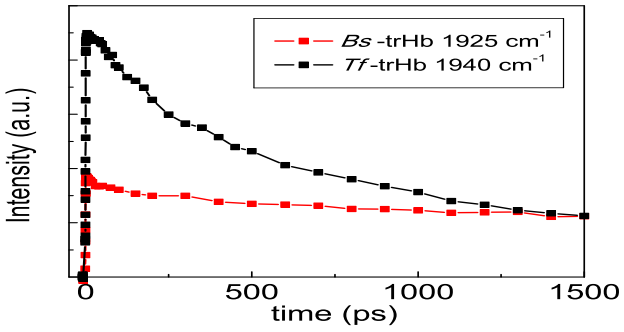


**Figure 4.16:** Comparison between the kinetic traces in the bleaching region for *Tf*-trHb and *Bs*-trHb upon excitation at 550 nm. Trace at 1940 cm$^{-1}$ of *Tf*-trHb (black line) is compared to the trace at 1925 cm$^{-1}$ of *Bs*-trHb (red line). The two kinetic traces have been scaled to overlap on the long time scale.

For both proteins two different conformations have been identified, herein referred as an 'open' conformation, characterized by a single amino acid H-bonded to the ligand and a 'closed' conforma-

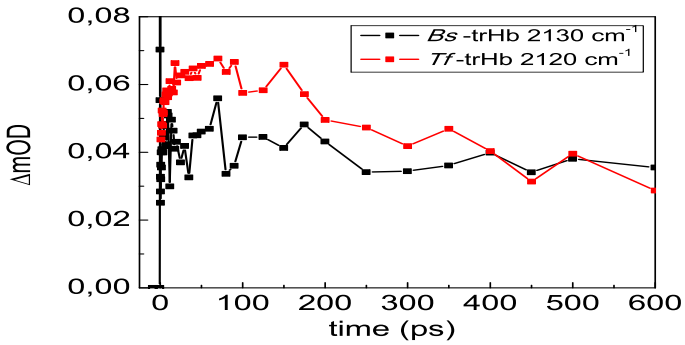


**Figure 4.17:** Kinetic trace at 2120 $cm^{-1}$ recorded at the maximum absorption in the free CO region in *Tf*-trHb (red line) compared with the corresponding kinetic trace measured in *Bs*-trHb at 2130 $cm^{-1}$ (black line).

tion, with two H-bonded residues [43, 48]. In the case of *Tf*-trHb, the dynamics of bleaching recovery of the 'open' and 'closed' conformations are different. The 'open' conformation, responsible for the infrared band at 1940 $cm^{-1}$ substantially recovers with a fast 250 ps component, while for the 'closed' one the picosecond component only accounts for a minor fraction of signal recovery. It is commonly accepted in the literature that the presence of H-bonds between the residues in the distal pocket and the heme bound CO favors the occurrence of fast recombination. For instance it was recently shown that in the oxygen sensory protein FixL the introduction of a residue capable of forming H-bonds with the iron bound CO, through the mutation R220H, determines the occurrence of substantial contribution to geminate recombination on a 250 ps time scale [109, 115]. On that basis one would expect to observe substantial amount of picosecond geminate recombination also in *Bs*-trHb, since, for this protein, the highly downshifted $\nu$(CO) stretching measured by FT-IR indicated the presence of strong H-bonds between the iron coordinated CO and the residues in the distal pocket. Nevertheless our results show that

only a minor fraction of the photolized CO, corresponding to less than 10% of the total, recombines with a 120 ps kinetics. The fraction of the fast dynamic phase is the same for both the 'open' and 'closed' conformations of the protein, being thus independent of the number of H-bonds formed by the coordinated ligand. We also note that, in *Tf*-trHb, the higher fraction of fast recombination is observed in the 'open' conformation, i.e. the one with only one H-bond and not, as it would be expected at a first sight, when both TyrCD1 and TrpG8 are H-bonded to the coordinated CO. A similar behavior has been observed in the case of myoglobin, in which time resolved infrared spectra measured at low temperature showed the appearance of two bleaching bands (at 1944 and 1926 $cm^{-1}$), recovering on a different time scale. Even in this case the higher frequency band, corresponding to an 'open' configuration, recovers faster than the low frequency one, like in *Tf*-trHb [27]. By comparing the behavior of the two truncated hemoglobins here studied, it can be suggested that one of the main factors influencing the amount of fast geminate recombination is the structural flexibility of the heme pocket. The steric hindrance of the residues surrounding the ligand, which can act as a cage confining the CO in the docking site, avoids its escape towards the solvent. If the docking site of the photolyzed CO is sufficiently large, because of the presence of smaller residues in the distal pocket, the recombination is slower. On the contrary if bulky residues prevent ligand escape, the CO molecule may possibly recombine with the iron atom on a faster time scale. These observations are still not sufficient to explain the different dynamics observed for the two conformations of *Tf*-trHb. In this protein, the residue TyrCD1, which in the 'closed' conformation is at H-bond distance from the iron coordinated CO, is believed to have a high structural flexibility, being alternatively capable of forming a H-bond either with a water molecule localized in its proximity or with the ligated CO. It would be expected that, when this residue is

rotated towards the ligand, as in the 'closed' conformation, it would prevents the photolyzed CO to escape far from the heme. In the 'open' conformation TyrCD1 is rotated away from the ligand instead, so it may allow the CO molecule to move further away from the heme upon photolysis. In contrast, in the experimental conditions used in this work, we observe a faster rebinding for the 'open' conformation. This may indicate that the differences among the two protein conformations can involve more significant rearrangements than TyrCD1 rotation. One possibility is that when TyrCD1 is rotated away from the ligand, the conserved water molecule located in the distal site assumes a position such to block the CO exit. Alternatively there could be rearrangements in the position of other residues, not identified in the currently available crystal structure, acquired without coordinated CO [46], which eventually make the 'open' conformation even more restrained than the 'closed' one. It thus appears that in case of this protein it is not totally correct to refer to the two conformations as 'open' or 'closed' only considering the number of hydrogen bonds formed with the iron-bound CO, while it would be more appropriate to identify them as a less constraining and more constraining conformation. For *Bs*-trHb, until now, we have described the 'closed' conformation as the one where both TrpG8 and TyrB10 are H-bonded to the ligand, and the 'open' conformation as the one where only the H-bond with TrpG8 is maintained. In this case there is little difference in the dynamics of CO recombination between them. Possibly, the configuration adopted by TrpG8 and the other pocket residues is not very different for the two conformations, so that the volume of the docking cavity is unchanged. Furthermore the other residue which is located in the distal pocket of *Bs*-trHb at short distance from the coordinated CO is GlnE11, whose hindrance is certainly reduced if compared to that of TyrB10 which in *Tf*-trHb is also at short distance from the CO, besides TrpG8 and TyrCD1. It is worth noting

that the importance of GlnE11 in stabilizing the coordinated ligand in *Bs*-trHb has been recently highlighted. According to molecular dynamic simulations, GlnE11 can adopt two different conformations, forming a H-bond alternatively either with the iron bound CO or with TyrB10 [116]. By switching among these two conformations GlnE11 would open a cavity directly connecting the heme distal pocket with the solvent, thus favoring ligand escape. This finding would explain the high oxygen affinity observed for *Bs*-trHb and strengthens the suggestion that the volume of the heme cavity and its structural flexibility have a strong influences on the fraction of fast geminate recombination [116]. Compared to *Tf*-trHb, in this case there is less protein reorganization after photolysis, possibly because the docking site is already sufficiently large to accommodate the dissociated ligand, due to the topological substitution between TyrCD1 with PheCD1 and LeuE11 with GlnE11. A lower degree of protein rearrangement induced by the ligand dissociation could also explain the absence of a rise component in the kinetics of the photodissociated CO. Similar considerations regarding the 'caging' effect [117, 44], played by the amino-acid residues surrounding the photolyzed CO can also be applied to other recently studied systems. Picosecond geminate recombination has also been found in the CO complex of non-globin proteins, such as microperoxidase and in the chemically modified form of cytochrome c, termed carboxymethyl cytochrome c [118]. In the former system a time constant of 110 ps has been estimated for samples at high concentration [40], while in the latter system a multiphasic recombination with time constant of 16 ps, 120 ps and 1 ns has been measured [41]. The authors attributed the three phases to CO rebinding from different locations within the distal pocket site. The high efficiency of the ligand rebinding has been interpreted even in this case as a consequence of a sterically hindered and 'caged' nature of the distal heme pocket, from which it is difficult for the ligand to escape. In these systems,

the short timescale of the geminate rebinding has been correlated to a protein configuration that assures the restraint of the reorganization energy of the active site [41]. As a final comment, it should be pointed out that the kinetic analysis presented until now does not take into account that a fraction of the photolyzed CO escapes to the solvent, and recombines on a much longer time scale with a bimolecular process. A direct estimation of the relative amount of geminate and bimolecular recombination would require to follow the system dynamics on a time scale spanning from pico to milliseconds, which is not feasible with the currently used experimental set-up. However, it is possible to have an estimate of the amount of geminate recombination occurring on the picoseconds time scale by evaluating the ratio between the areas of the EADS obtained by global analysis. In the case of *Tf*-trHb it can be estimated that about 40% of CO undergoes picosecond geminate recombination. The evaluation of kinetic component in the nanosecond regime is affected by a large (about 20%) indetermination due to the lack of data regarding the bi-molecular recombination. Our results highlight striking differences between the dynamics of CO recombination in the truncated hemoglobins with respect to other globins, such as vertebrate myoglobins and hemoglobins. Both the truncated hemoglobins from *Thermobifida fusca* and *Bacillus subtilis* exhibit sub-nanosecond multiexponential geminate recombination, which account for at least 50% of the total yield of CO recombination. The occurrence of fast geminate rebinding and the differences in the CO rebinding kinetics registered for two apparently similar proteins highlight the strong influence played by the structural organization of the distal heme pocket and the interactions among the protein and the heme-ligand complex.

## 4.5 3F-*Tf*-trHb

To complete the present study we performed time-resolved infrared experiments on the mutant protein 3F-*Tf*-trHb in order to understand how distal heme pocket structural changes can affect CO recombination dynamics in *Tf*-trHb.

### 4.5.1 Steady State Spectra

The UV-Vis spectrum of 3F-*Tf*-trHb-CO complex is reported in Fig.4.18.

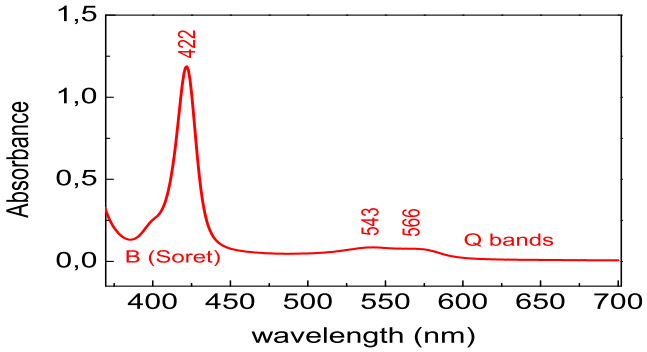


**Figure 4.18:** UV-Visible spectrum of 3F-*Tf*-trHb-CO complex. Protein solution was prepared by dissolving the lyophilized protein in a TRIS-HCl buffer 0.2 M in $D_2O$ (pD=8). The concentration of 3F-*Tf*-trHb was 13 mM, the cell pathlength 50$\mu$m. CO was added after protein reduction with sodium dithionite (for more details see section 2.2.6).

The FT-IR spectrum of the 3F-*Tf*-trHb-CO complex is shown in Fig.4.19. Only one band centered at 1955 cm$^{-1}$ is present as no hydrogen bonds, capable to stabilize the iron-bound CO, are formed.

### 4.5.2 Time Resolved Mid-IR Spectra

In order to investigate the CO recombination dynamics in 3F-*Tf*-trHb with UV-Vis-pump mid-IR-probe we have triggered ligand dis-

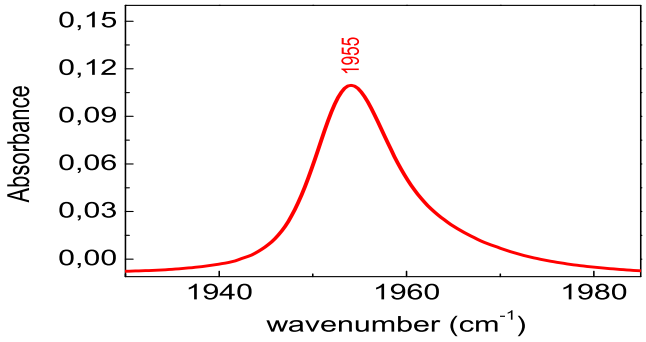


**Figure 4.19:** FT-IR spectrum of 3F-*Tf*-trHb-CO complex. Protein solution was prepared by dissolving the lyophilized protein in a TRIS-HCl buffer 0.2 M in $D_2O$ (pD=8). The concentration of 3F-*Tf*-trHb was 13 mM, the cell pathlength 50$\mu$m. CO was added after protein reduction with sodium dithionite (for more details see section 2.2.6).

sociation with 550 nm visible pump pulses. We have monitored CO rebinding in two mid-IR regions: the region of the $\nu$(CO) stretching vibration of the iron-bound CO (1880-1980 $cm^{-1}$) and the dissociated free CO absorption region (2030-2230 $cm^{-1}$).

### *Bound CO*

Time resolved spectra of 3F-*Tf*-trHb in the bleaching region were collected by exciting the sample using 550 nm pump pulse and are reported in Fig.4.20. Following CO photodissociation, only one bleaching band is observed at 1955 $cm^{-1}$ which position well correspond with the measured FT-IR spectrum of the CO adduct for this protein (Fig.4.19).

The global analysis of the kinetic traces, using a sequential model scheme, has revealed a bi-phasic recovery occurring within a sub-nanosecond timescale. The kinetic trace taken at the maximum of the bleaching band is reported in Fig.4.21.

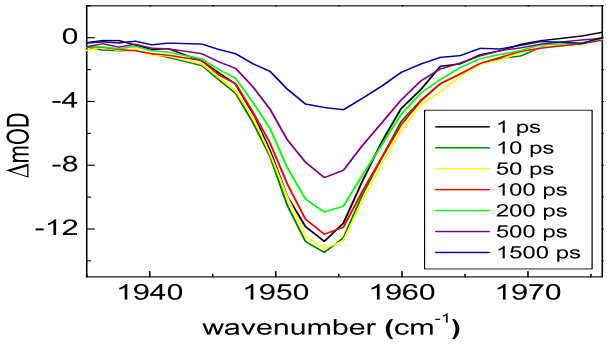


**Figure 4.20:** Time resolved spectra recorded at different time delays, showing the bleaching induced by the excitation at 550 nm in the $\nu$(CO) stretching region for the iron-bound CO.

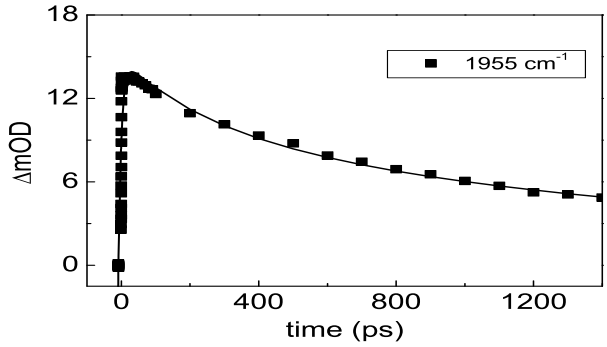


**Figure 4.21:** Kinetic trace (scattered points) at 1955 cm$^{-1}$ with the fit (solid line) obtained by global analysis.

The kinetic trace can be satisfactorily fitted with two components, whose time constants are 250 ps and 1.4 ns, respectively. This kinetic behavior is similar to that observed for the WT protein but the fast picosecond component seems to account for a minor fraction of the total recombination process respect to *Tf*-trHb. This observation will

be discussed in detail in the next section.

### *Dissociated CO*

Measurements were carried out by setting the excitation pulse at 550 nm, probing the stretching region for free CO absorption from 2030 to 2230 $cm^{-1}$.

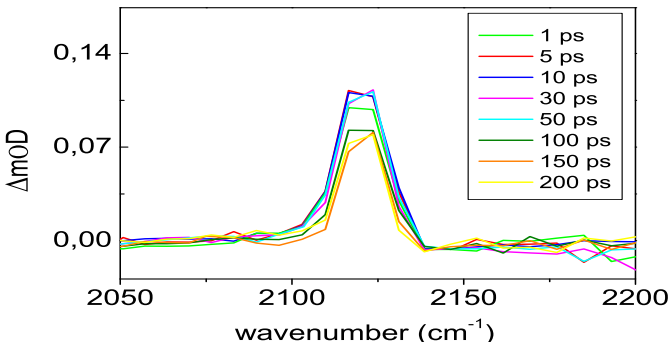


**Figure 4.22:** Time resolved spectra in the free CO region recorded at different time delays after excitation of the sample with a 550 nm laser pulse.

Spectra in Fig.4.22 have been corrected, as in previous cases, for the presence of a baseline which contributes to the signal. The FWHM average value found for the free CO absorption bands of the mutated protein is about 15 $cm^{-1}$, a value about the half of the observed value for the WT protein ($\approx$ 25 $cm^{-1}$); this finding highlights the fact that the molecular environment has been radically changed by the triple Phe mutation (this topic will be treated in depth in the next section). Fig.4.23 shows the kinetic trace measured at the absorption maximum of the free CO signal compared with that of the 1955 $cm^{-1}$ bleaching band. The two kinetic traces have been scaled to be appropriately compared. The two kinetic traces are in good agreement confirming that the 250 ps time constant is relative to the fast geminate recom-

bination.

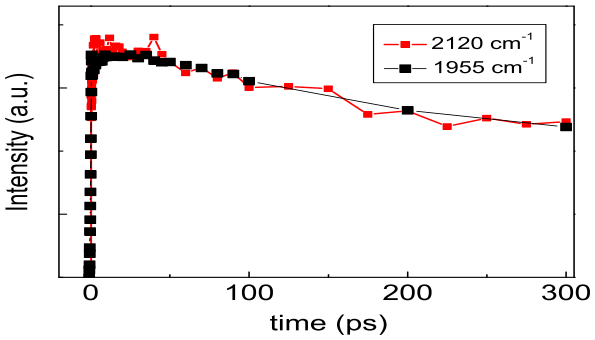


**Figure 4.23:** Kinetic traces at 2120 cm$^{-1}$ (red line), corresponding to the maximum absorption in the free CO region in 3F-*Tf*-trHb. The trace has been superimposed with the kinetic trace at 1955 cm$^{-1}$ (black line), corresponding to the maximum absorption of the coordinated CO.

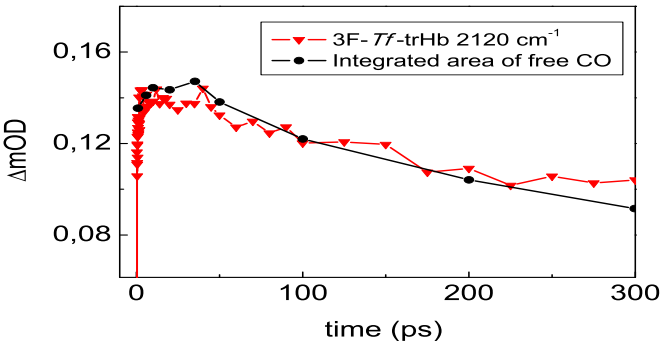


**Figure 4.24:** Comparison between the kinetic trace at 2120 cm$^{-1}$, corresponding to the peak of the free CO absorption band (red line) and the time evolution of the integrated area of the full CO absorption band (black line).

In order to take into account the bandwidth variation with time, we estimated the temporal evolution of the integrated area of the

CO band, and we compared it with the kinetic trace at 2120 $cm^{-1}$, corresponding to the band maximum. The two traces are in good agreement (Fig.4.24).

## 4.6 Comparison Between *Tf*-trHb and 3F-*Tf*-trHb

In the second part of this study we have compared *Thermobifida fusca* trHb and its triple mutant 3F-*Tf*-trHb in which the three foundamental amino acids, responsible for the ligand stabilization through the formation of a H-bond network (TyrB10 TyrCD1 and TrpG8), have been replaced by Phe residues. We expected that the triple mutation would have had a very strong effect on the dynamics of recombination of CO. Present results indicate that although both proteins show fast geminate recombination, the relative amount of the picosecond dynamic phase is not the same. In order to highlight these differences we have compared in Fig.4.25 the kinetic traces measured for the two bleaching bands of *Tf*-trHb (1940 and 1920 $cm^{-1}$) with the kinetic trace corresponding to bleaching band observed for 3F-*Tf*-trHb (1955 $cm^{-1}$). The curves have been normalized on the long (ns) time scale component. This procedure is quite arbitrary; however it allows to highlight the differences between the three signals.

The observed signals bring out clearly a faster decay in the case of 1940 $cm^{-1}$ component of *Tf*-trHb with respect to that at 1955 $cm^{-1}$ of 3F-*Tf*-trHb. Instead the kinetic trace taken at 1920 $cm^{-1}$ of *Tf*-trHb presents a similar kinetic behavior with respect to the 1955 $cm^{-1}$ trace of the mutant protein. We tried to estimate the relative weights of the fast component in the three kinetic traces but the evaluation of kinetic components in the nanosecond regime is affected by a large (about 20%) indetermination due to the lack of data regarding the bimolecular recombination. The two bleaching bands observed in the MIR spectrum for *Tf*-trHb are relative to two different populations

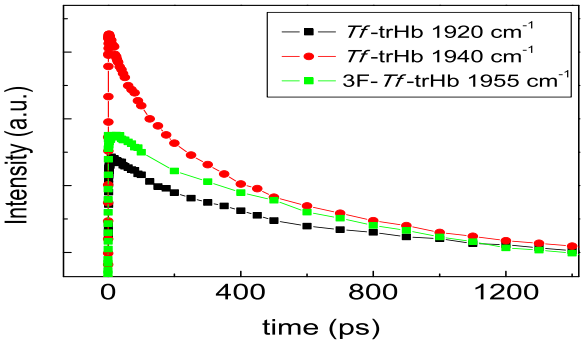


**Figure 4.25:** Comparison between the kinetic traces in the bleaching region for *Tf*-trHb and 3F-*Tf*-trHb upon excitation at 550 nm. Traces at 1940 cm$^{-1}$ (red line) and 1920 cm$^{-1}$ (black line) of *Tf*-trHb are compared to the trace at 1955 cm$^{-1}$ of 3F-*Tf*-trHb (green line). The three kinetic traces have been normalized on the long time scale.

which do not interconvert in the temporal regime that we have analyzed. In *Tf*-trHb the presence of a ligand inclusive hydrogen bond network, in which the three polar amino acids TrpG8, TyrCD1 and TyrB10 are mostly implicated, represents a considerable barrier to ligand escape, in fact an efficient geminate rebinding has been observed. The comparison of the three kinetics traces in Fig.4.25 highlights that the rebinding of CO on a time scale of picoseconds is more predominant in the WT protein than in the mutant protein. In particular the 'open' conformation in which CO only is stabilized by a hydrogen bond with TrpG8 (1940 cm$^{-1}$ band) shows a kinetic in which the fast component has a very high weight (about 40%). As mentioned before, in the open conformation the TyrCD1, not involved in the stabilization of CO, is capable of forming a bond with the water molecule which is located in its proximity within the pocket. In this conformation the water molecule plays an important role in mantaining the CO close to the heme iron by restricting the effective distal pocket volume

making easier its rapid rebinding. In the 'closed' conformation CO is doubly H-bonded to both TrpG8 and TyrCD1 (1920 $cm^{-1}$ band) and the water molecule is free. In this situation the caging effect on the CO molecule could be less constraining and we observe a kinetic behavior in which the time component in the picosecond regime has a much less marked effect on the overall process compared to what happens in the closed conformation (1940 $cm^{-1}$). The role of a single water molecule is tremendously important in determining the ratio between fast and intermediate geminate recombination and makes the WT protein very sensitive to small variations in the experimental conditions. In 3F-*Tf*-trHb no stabilization of the CO via formation of hydrogen bonds is possible; moreover the conserved water molecule is not present in its apolar heme pocket; the only conformer with the heme-bound CO conrespond to the band located at 1955 $cm^{-1}$. The ultrafast geminate rebinding, in this mutant protein, is remarkably strong despite the absence of the hydrogen-bonding network in the distal pocket and the reactivity of dissociated CO towards the heme is not strongly changed. Moreover in 3F-*Tf*-trHb the conserved water molecule is not present and it cannot form H-bond with TyrCD1 thus probably the distal pocket could become less constraining against the ligand that in the native protein. Similar findings have been reported for *Mycobacterium tubercolosis* trHbO by Vos and coworkers [119]. Using femtosecond spectroscopy, the authors analyzed the WT trHbO and two single and one double mutants in which the conserved amino acids of distal heme pocket TrpG8 (Trp88), TyrCD1 (Tyr36) have been replaced with Phe residues. They found that CO rebinding occurs for 95% predominantly in 1.2 ns in all the analyzed proteins. The rebinding properties were unexpectedly robust against the mutations of the distal pocket residues (the mutants all showed an additional decay phase of 250 ps respect to the WT protein) and the interaction of the ligand with structural water molecules as well as its rotational

freedom played a role in the high reactivity of the ligand toward the heme.

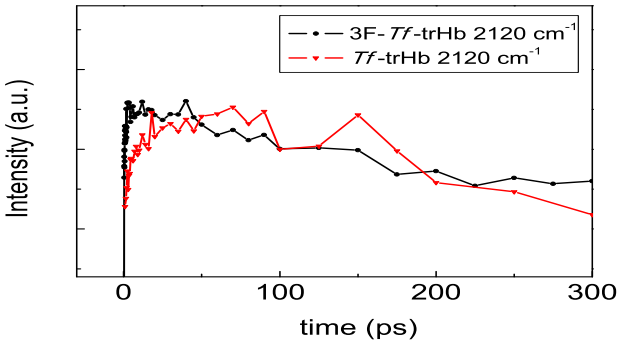


**Figure 4.26:** Kinetic trace at 2120 cm$^{-1}$ recorded at the maximum absorption in the free CO region in *Tf*-trHb (red line) compared with the corresponding kinetic trace measured in 3F-*Tf*-trHb at 2120 cm$^{-1}$ (black line) in the first 300 ps.

In Fig.4.26 the kinetic traces correspondig to the maximum of the free CO absorption bands for *Tf*-trHb and 3F-*Tf*-trHb are reported. The dinamical evolution of the two signals is similar except for the first 30 ps, in fact for the WT protein a rise component is present on this time scale. We have attributed this 30 ps component to significant protein rearrangement involving the rotation or reorientation of one or more aminoacid side chains in the CO docking site. We have not observed this component in neither of the two other proteins studied and this can be correlated to the fact that *Tf*-trHb heme pocket is more flexible then those of the other two proteins and to the the fact that it contains a water molecule which creates a more eterogeneous environment for the dissociated CO molecule. In particular, in 3F-*Tf*-trHb the environment within the distal heme pocket is more apolar and more homogeneous than that of the WT protein. A lower degree of protein rearrangement induced by the ligand dissociation could explain the absence of a rise component in the kinetics of the

photodissociated CO in 3F-*Tf*-trHb and *Bs*-trHb.

## 4.7 Free CO Band Shape as a Function of Chemical Environment: a Qualitative Comparison

The free CO absorption bands of the three analyzed protein, normalized to the same intensity to make easier the comparison between them, and recordet at 30 ps delay time are reported in Fig.4.27. By modeling the curves with a Gaussian function, we have found a FWHM of $\approx 27$ cm$^{-1}$ for *Bs*-trHb and 25 cm$^{-1}$ for *Tf*-trHb while for triple mutated protein the value is almost halved ($\approx 15$ cm$^{-1}$). The CO absorption bands for *Tf*-trHb and 3F-*Tf*-trHb are centered at $\approx$ 2120 cm$^{-1}$ while for *Bs*-trHb the central frequency is located at $\approx$ 2130 cm$^{-1}$. The shifts relative to the gas frequency of CO ($\nu_0$=2143 cm$^{-1}$) are 13 cm$^{-1}$ in the case of *Bs*-trHb and 23 cm$^{-1}$ for the other two proteins. For MbCO three B states, $B_1$, $B'_2$ and $B"_2$ have been found [111] to be localized respectively at 2132, 2122 and 2117 cm$^{-1}$ and to have a FWHM of 9.1, 6 and 10.1 cm$^{-1}$; the shifts relative to the gas frequency for these states are found to be 11, 21.2 and 25.9 cm$^{-1}$ respectively. $B_1$ and $B_2$ have been attributed to CO located with opposite orientations toward the heme iron. In both rotamers the CO axis ligand is roughly parallel to the heme plane. The high frequency (2132 cm$^{-1}$) $B_1$ state was assigned to the conformer with the O atom pointing back toward the heme iron atom while the low frequency (2122 cm$^{-1}$) $B_2$ state to the opposite orientation.

The red shifts from value of 2143 cm$^{-1}$ for the gaseous CO imply weak interactions between the CO in the pocket and the residues constituting the distal heme pocket. The magnitude of the shift increases with binding enthalpy [120]. In myoglobin the shift of $B_0$ (2146 cm$^{-1}$) suggests that the CO is free inside the heme pocket while in $B_1$ and $B_2$ (2132 and 2122 cm$^{-1}$) it is weakly bound to the heme or to the

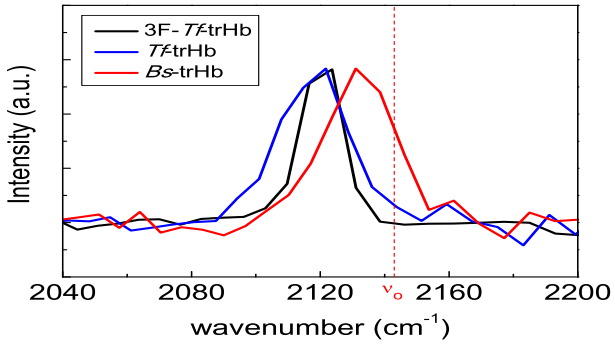


**Figure 4.27:** Free CO normalized spectra (obtained exciting the samples with 550 nm laser pulse) taken at 30 ps delay time for *Tf*-trHb, 3F-*Tf*-trHb and *Bs*-trHb. $\nu_0$ indicates the central frequency of the gaseous CO absorption band (2143 cm$^{-1}$).

aminoacidic residues of the heme wall [120]. The 2130 cm$^{-1}$ of *Bs*-trHb resembles the $B_1$ band of myoglobin and indicates a strong interaction between the dissociated CO and the distal residues; the distal heme pocket defines the environment of the iron-bound ligand as well as the environment of the ligand both immediately after dissociation and just prior to binding. In this view the distal pocket of *Bs*-trHb is characterized by polar residues and there is a strong stabilization of the bound CO that is confirmed by the very low C-O frequency stretching at 1888 cm$^{-1}$. This interaction plays a role also on the free CO molecule. *Tf*-trHb and its 3F mutant exhibit the free CO stretching band around 2120 cm$^{-1}$ and the shift relative to the gaseous CO is twice respect to *Bs*-trHb. *Tf*-trHb distal heme pocket is very similar to that of *Bs*-trHb; both pockets present TrpG8 and TyrB10, in case of *Bs*-trHb the distal pocket is completed by GlnE11, ThrE7, PheB9 and PheCD1 while in *Tf*-trHb there are LeuE11, TyrCD1, PheB9 and AlaE7; one important difference between the heme pockets of these two proteins is that in *Tf*-trHb heme pocket a water molecule is also

present. This water molecule, as mentioned before, could diminish the volume of the heme pocket and could form a narrower cage in respect to the free CO molecule. Under the line shape of the dissociated CO absorption bands of the three proteins the presence of two unresolved bands can be postulated taking into account the findings on Mb [111, 120, 40] but, considering our resolution (6 $cm^{-1}$) and the baseline fluctuation problems we cannot make any speculation about the presence of other states. In the case of 3F-*Tf*-trHb we have observed a very narrow absorption band respect to the WT protein. The substitution of the three polar amino acids TrpG8, TyrB10 and TyrCD1 of the WT protein with Phe residues leads to a non polar and more omogeneous distal pocket which could give rise to the more narrow band. The distal pocket environment becomes more ordered and less flexible than that of the WT and the band narrowness indicates that the CO is in a more constrained environment. In the two WT protein the distal heme pockets are higly polar and the photolyzed CO has broader bandwidths indicating that it sees a more polar surroundings and/or a less ordered and more flexible environment. Anyhow the free CO absorption bands within the proteins are narrower than that of CO dissolved in organic solvents; the shifts relative to the gaseous CO cental frequency are larger for the CO docked in the protein matrix respect to those observed for the CO dissolved in pure solvents. This can be either ascribed to specific interactions and/or to high values of viscosity within the protein matrix.

# Conclusions

The possibility to follow CO recombination dynamics, in the middle infrared spectral region, after photolysis induced by a short laser pulse provides unique information about the influence of structural and electrostatic properties of the distal heme pocket on the ligand dissociation and rebinding processes occurring in globin proteins. While pump-probe measurement in the visible spectral range gives only indirect information on the recombination dynamics, since they can only probe the evolution in the electronic state of the heme moiety after excitation, measurements in the infrared are much more specific, since they can probe the dynamics of the vibrational bands of the ligand before and after photolysis, thus providing a direct snapshot of the transient state of the photolyzed CO. In this work we have shown that, in the case of *Bs*-trHb, infrared probe has allowed to assign unambiguously a 30 ps component previously identified by visible transient absorption measurements. The absence of this kinetic component in the current measurements within the infrared spectral range, leads to the conclusion that it is not associated to fast ligand recombination, but more likely represents a relaxation process of the heme. Furthermore, important information on the influence of the distal pocket structure on the recombination dynamics can be retrieved with this technique. The presence of sub-nanosecond CO geminate rebinding (in all the three analyzed proteins) after photol-

ysis indicates that the dynamics of the ligand is confined within the distal pocket itself with a remote possibility of escape to the solvent or to the cavities of the protein matrix. The comparison between *Tf*-trHb and *Bs*-trHb has highlighted that in both proteins the polar aminoacid residues, capable to interact with the iron-coordinated CO through the formation of H-bonds, act as a cage on dissociated CO preventing its escape toward the solvent and favoring its fast rebinding. Moreover, different geminate recombination has been observed for 'open' and 'closed' conformations in *Tf*-trHb but not in *Bs*-trHb, indicating that the percentage of the fast rebinding process is not directly related to the number of H-bonds. Taken together, vibrational spectroscopy and dynamics data indicate that the active site of group II trHbs is not designed to perform gaseous ligand exchange and is more likely devoted to other catalytic processes such as NO detoxification and peroxidase-like activity. The analysis of the 3F-*Tf*-trHb has shown that the ultrafast geminate rebinding, in this mutant protein, is remarkably strong despite the absence of the hydrogen-bonding network and that the reactivity of dissociated CO towards the heme is not strongly changed by the mutation. The analysis of the free CO absorption band in the three proteins has shown that the substitution of the three polar amino acids TrpG8, TyrB10 and TyrCD1 of the WT protein with Phe residues leads to a non polar and more omogeneous distal pocket which gives rise to a more narrow CO band in the mutant protein respect to the two WT proteins. Furthermore the free CO absorption bands within the proteins are narrower than that observed for CO dissolved in organic solvents and the shifts relative to the gaseous CO central frequency are more pronounced for the CO docked in the protein matrix respect to the CO dissolved in solvents. These observations lead to conclude that the protein matrix and expecially the heme pocket flexibility play a very important role in controlling the reactivity of the active site respect to the exogenous

ligands.

# Bibliography

[1] H.M. Dintzis R.G. Parrish H. Wyckoff D.C. Phillips J.C. Kendrew, G. Bodo. *Nature*, 181, 662, 1958.

[2] X. Bailly R. Arredondo-Peter J. Gough S. Dewilde L. Moens J.R. Vanfleteren S.N. Vinogradov, D. Hoogewijs. *BMC Evol. Biol.*, 7, 31, 2006.

[3] T. Takagi. *Opinion Struct. Biol.*, 3, 77, 1993.

[4] R. Ebel D. Bassam M. Potts, S. Angeloni. *Science*, 256, 1690, 1992.

[5] T. Gorr J. Colacino-A. Riggs T. Vandergon, C. Riggs. *J. Biol. Chem.*, 273, 16998, 1998.

[6] B.A. Wittenberg J.B. Wittenberg-Y. Ouellet D. Rousseau M. Guertin M. Couture, S. Yeh. *Proc. Natl. Acad. Sci. USA*, 96, 11223, 1999.

[7] B.A. Wittenberg M. Guertin J.B. Wittenberg, M. Bolognesi. *J. Biol. Chem.*, 277, 871, 2002.

[8] B. St-Pierre J. Lafontaine M. Guertin M. Couture, H. Chamberland. *Mol. Gen. Genet.*, 243, 185, 1994.

[9] A. Hvitved-M. Hargrove W. Peacock E. Dennis R. Watts, P. Hunt. *Proc. Natl. Acad. Sci. USA*, 98, 10119, 2001.

[10] Michael C. Marden Henri Wajcman, Laurent Kiger. *C. R. Biologies*, 332, 273, 2009.

[11] Cutruzzola F. Savino C. Travaglini-Allocatelli C. Vallone B. Brunori, M. and Gibson Q. H. *Trends Biochem. Sci.*, 24, 253, 1999.

[12] Dewilde S. Guertin M. Yamauchi K. Ascenzi P. Moens L. Pesce A., Couture M. and Bolognesi M. *EMBO J.*, 19, 2424, 2000.

[13] Ouellet Y. Ascenzi P. Guertin M. Milani M., Pesce A. and Bolognesi M. *EMBO J.*, 20, 3902, 2001.

[14] Savard P.Y. Ouellet H. Ascenzi P. Guertin M. Milani, M. and M. Bolognesi. *Proc. Natl. Acad. Sci.*, 100, 5766, 2003.

[15] Kundu S. Trent J. T. Ramaswamy S. Hoy, J. A. and M. S. Hargrove. *J. Am. Chem. Soc.*, 279, 16535, 2004.

[16] Nardini M. Milani M. Pesce, A. and M. Bolognesi. *Life*, 59, 535, 2007.

[17] Dreuw A. Dunietz, B. D. and M. J. Head-Gordon. *Phys. Chem. B*, 107, 5623, 2003.

[18] Demidov A. Ye, X. and P. M. Champion. *J. Am. Chem. Soc.*, 124, 5914, 2002.

[19] J.-L. Martin and M. H. Vos. *Annu. Rev. Biophys. Biomol. Struct.*, 21, 199, 1992.

[20] R.B. Hu S.G. Boxer E.S. Park, S.S. Andrews. *J. Phys. Chem. B*, 103, 9813, 1999.

[21] T.G. Spiro and I.H. Wasbotten. *J. Inorg. Biochem.*, 99, 34, 2005.

[22] N.T. Yu E.A. Kerr. Biological applications of raman spectroscopy. *Spiro, T. G., Ed. Wiley-Interscience, New York*, vol. 3, 39, 1988.

[23] John S. Olson Barry A. Springer, Stephen G. Sligar and Jr. George N. Phillips. *Chemical Reviews*, 94(3), 699, 1994.

[24] George N. Phillips Jr. Tiansheng Li, Michael L. Quillin and John S. Olson. *Biochemistry*, 33, 1433, 1994.

[25] Braunstein D.P. Chu K. Frauenfelder H. Nienhaus G.U. Ormos P. Mourant, J.R. and R.D. Young. *Biophys. J.*, 65, 1496, 1993.

[26] X. Y. Li and T. G. Spiro. *J. Am. Chem. Soc.*, 110, 6024, 1988.

[27] P. A.; Hochstrasser R. M. Moore, J. N.; Hansen. *Proc. Nat. Acad. Sci.*, 85 (14), 5062, 1988.

[28] M. H. Vos. *Biochim. Biophys. Acta*, 1777, 15, 2008.

[29] E.R. Henry W.A. Eaton J. Hofrichter, J.H. Sommer. *Proc. Natl. Acad. Sci. U. S. A.*, 80, 2235, 1983.

[30] P.A. Anfinrud M. Lim, T.A. Jackson. *Nat. Struct. Biol.*, 4, 209, 1997.

[31] Stefan Franzen Karin Nienhaus, John S. Olson and G. Ulrich Nienhaus. *J. AM. CHEM. SOC.*, 127, 40, 2005.

[32] J. P.; Franzen S.; Vos M. H.; Joffre M.; Martin J. L.; Alexandrou A. Polack, T.; Ogilvie. *Phys. Rev. Lett.*, 93 (1), 018102, 2004.

[33] Lim M. Jackson T. A. Smirnov A. V. Soman J. Olson J. S. Phillips G. N. Wulff M. Schotte, F. and Anfinrud P.A. *Science*, 300, 1944, 2003.

[34] Anselmi M. Roccatano D. Amadei A. Vallone B. Brunori M. Bossa, C. and A. Di Nola. *Biophys. J.*, 86, 3855, 2004.

[35] Di Nola A. Anselmi, M. and A. Amadei. *Biophys. J.*, 94, 4277, 2008.

[36] R. Regan R. Elber J. S. Olson Gibson, Q. H. and T.E. Carver. *J. Biol. Chem.*, 267,22022, 1992.

[37] R. Elber Li, H. and J. E. Straub. *J. Biol. Chem.*, 268, 17908, 1993.

[38] D. Kunz Tilton, R. F. and G. A. Petsko. *Biochemistry*, 23, 2849, 1984.

[39] Steele A. W. Chernoff D. A. Cornelius, P. A. and R. M. Hochstrasser. *Proc. Natl. Acad. Sci.*, 78, 7526, 1981.

[40] Jackson T. A. Lim, M. H. and Anfinrud P. A. *J. Biol. Inorg. Chem.*, 2, 531, 1997.

[41] Jasaitis A. Vos M. H. Silkstone, G. and M. T. Wilson. *Dalton Trans.*, 21, 3489, 2005.

[42] Juszczak L. Dantsker D. Samuni U. Ouellet Y. H. B. Wittenberg B. A. Friedman J. M. Ouellet, H. and M. Guertin. *Biochemistry*, 42, 5764, 2003.

[43] Feis A. Catacchio B. Brogioni S. Foggi P. Chiancone E. Boffi A. Lapini, A. and G. Smulevich. *Biochemistry*, 47, 902, 2008.

[44] H.; Lambry J.-C.; Martin J.-L.; Friedman J. M.; Guertin M.; Vos M. H. Jasaitis, A.; Ouellet. *Chem. Phys.*, 396, 10, 2012.

[45] Abbruzzetti A. Bustamante J.P.-Feis A. Bonamore-A. Boffi A. Gellini C. Salvi P.R. Estrin D.A. Bruno S. Viappiani C. Foggi P. Marcelli, A. *PLoSE ONE*, 7(7), e39884, 2012.

[46] Ilari A. Giangiacomo L.-Bellelli A. Morea-V. Bonamore, A. and A. Boffi. *FEBS Lett.*, 272, 4189, 2005.

[47] Huang C. C.-Couch G. S. Greenblatt D. M. Meng E. C. Ferrin T. E. Pettersen E. F., Goddard T. D. Ucsf chimera-a visualization system for exploratory research and analysis. *J. Comput. Chem.*, 25, 1605, 2004.

[48] F. P.; Bonamore A.; Boechi L.; Arroyo Mañez P.; Estrin D. A.; Boffi A.; Smulevich G.; Feis A. Droghetti, E.; Nicoletti. *Biochemistry*, 49 (49), 10394, 2010.

[49] A. Bonamore L. Boechi F. M. Boubeta A. Feis G. Smulevich F. P. Nicoletti, A. Comandini and A. Boffi. *Biochemistry*, 49, 2269, 2010.

[50] Hou S. Dioum E. M. Saito J. A. Newhouse J. Gonzalez G. Gilles-Gonzalez M. A. Freitas, T. A. and M. Alam. *Proc. Natl. Acad. Sci. U. S. A.*, 101, 6675, 2004.

[51] Boffi A. Morea V. Chiancone E. Giangiacomo L., Ilari A. *J. Biol. Chem.*, 280, 9192, 2005.

[52] Ouellet Y. Guertin M. Friedman J. M. and Yeh S. R. Samuni, U. *J. Am. Chem. Soc.*, 126, 2682, 2004.

[53] M. Gouterman. The porphyrins. *D. Dolphin, Ed. Academic Press.*, 1979.

[54] M. P. Marzocchi and G. Smulevich. *J. Raman Spectr.*, 34, 725, 2003.

[55] M. Zerner and M. Gouterman. *Theoret. Chim. Acta (Berlin)*, 4, 44, 1996.

[56] Kirmaier C. Dixon, D. W. and D. Holten. *J. Am. Chem. Soc.*, 107, 808, 1985.

[57] Kilmaier C. Rodriguez, J. and D. Holten. *J. Am. Chem. Soc.*, 111, 6500, 1989.

[58] Kilmaier C. Rodriguez, J. and D. Holten. *J. Chem. Phys.*, 94, 6020, 1991.

[59] C. V. Shank and E. P. Ippen. *Science*, 193, 50, 1976.

[60] Hanson L. K. Stephens P. J. Sutherland J. C. Eaton, W. A. and J. B. R. Dunn. *J. Am. Chem. Soc.*, 100, 4991, 1978.

[61] Migus A. Poyart C. Lecarpentier Y. Astier R. Martin, J.-L. and A. Antonetti. *Proc. Natl. Acad. Sci.*, 80, 173, 1983.

[62] Martin J.-L. Houde D. Poyart C. Petrich, J. W. and A. Orszag. *Biochemistry*, 26, 7914, 1987.

[63] Kiger L. Poyart-C. Franzen, S. and J.-L. Martin. *Biophys. J.*, 80, 2372, 2001.

[64] Volk M. Gooding-E. Kholodenko, Y. and R. M. Hochstrasser. *Chem. Phys.*, 259, 71, 2000.

[65] Jackson T. A. Lim, M. H. and P. A. Anfinrud. *J. Phys. Chem.*, 100, 12043, 1996.

[66] J. N. J. Harvey. *Am. Chem. Soc.*, 122, 12401, 2000.

[67] D. E. Sagnella and J. E. Straub. *J. Phys. Chem. B*, 105, 7057, 2001.

[68] Dunietz B. D. Dreuw, A. and M. Head-Gordon. *J. Am. Chem. Soc.*, 124, 12070, 2002.

[69] Dunietz B. Dreuw A. Head-Gordon M. Ugalde, J. M. and R. J. Boyd. *J. Phys. Chem. A*, 108, 4653, 2004.

[70] Demidov A. Rosca F. Wang W.-Kumar A. Ionascu D. Zhu L. Barrick D.-Wharton D. Ye, X. and P. M. Champion. *J. Phys. Chem. A*, 107, 8156, 2003.

[71] Sundström. Femtochemistry and femtobiology. *Imperial College Press, London*, 1977.

[72] M. H. Vos J.-L. Martin. *Annu. Rev. Biophys. Biomol, Struct.*, 21, 199, 1992.

[73] Diem M. Biophysical applications of vibrational spectroscopy, in introduction to modern vibrational spectroscopy. *New York: John Wiley Sons*, 204-235, 1993.

[74] Caughey W. S. Dong A. *Methods Enzymol.*, 232, 139, 1994.

[75] Y. R. Shen. The principles of nonlinear optics. *Wiley: New York*, 1984.

[76] S. Mukamel. Principles of non-linear optical spectroscopy. *Oxford University Press, USA*, 1995.

[77] R. M. Wynne, K.; Hochstrasser. *Chemical Physics*, 193(3), 211, 1995.

[78] P. Hamm. *Chemical Physics*, 3,415, 1995.

[79] D.; Migus A.; Antonetti A.; la Guillaume C. B. a.; Peyghambarian N.; Lindberg-M.; Koch S. W. Joffre, M.; Hulin. *Opt. Lett.*, 13(4), 276, 1988.

[80] P.T. Touceda M. Lima A. Lapini, S.M. Vázquez. *Journal of Molecular Structure*, v.993, iss.1-3, 470, 2011.

[81] R. L. Sutherland. Handbook of non-linear optics. *Marcel Dekker Inc*, 1996.

[82] R. Alfano. The supercontinuum laser source. *Springer-Verlag Berlin and Heidelberg GmbH Co. K*, 1989.

[83] P. L.; Alfano R. R. Agrawal, G. P.; Baldeck. *Phys. Rev. A*, 40(9), 5063, 1989.

[84] H. In Wolf E. Brunner, W.; Paul. Ed., progress in optics xv. *North-Holland*, Vol.XV, 1977.

[85] G.; Nikogosyan D. Dmitriev, V.; Gurzadyan. Handbook of nonlinear optical crystals. *Springer Series in Optical Science; Springer, third ed.*, 64, 1999.

[86] F.; Noack F. Petrov, V.; Rotermund. *Journal of Optics A: Pure and Applied Optics*, 3(3), R1, 2001.

[87] R. A.; Stenger J. Hamm, P.; Kaindl. *Opt. Lett.*, 25, 1798, 2000.

[88] V.; Noack F. Rotermund, F.; Petrov. *Optics Communications*, 185(1-3), 177, 2000.

[89] M.; Reimann K.; Hamm P.; Weiner A. M.; Woerner M. Kaindl, R. A.; Wurm. *J. Opt. Soc. Am. B*, 17(12), 2086, 2000.

[90] M.; Hubner H.-J.; Kaiser W. Seilmeier, A.; Worner. *Applied Physics Letters*, 53(25), 2468, 1988.

[91] T. A.; Anfinrud-P. A. Lim, M.; Jackson. *J. Am. Chem. Soc.*, 126 (25), 7946, 2004.

[92] Rajagopal S. Ren Z. Schmidt, M. and K. Moffat. *Biophys. J.*, 84, 2112, 2002.

[93] Y.; Locke B.; Hochstrasser R. M. Lian, T.; Kholodenko. *The Journal of Physical Chemistry*, (19), 7272, 1995.

[94] R. I. Hendler, R. W.; Shrager. *Journal of Biochemical and Biophysical Methods*, 28 (1), 1, 1994.

[95] J.; Ludwig Brand M. L. J. Henry, E. R.; Hofrichter. Singular value decomposition: Application to analysis of experimental data. *In Methods in Enzimology*, Academic Press: 1992; Vol.210, 129, 1992.

[96] E. R. Henry. *Biophysical journal*, 72 (2), 652, 1997.

[97] A. K. Dioumaev. *Biophys. Chem.*, 67, 1, 1997.

[98] J.; Zuberbuhler A. D. Bonneau, R.; Wirz. *Pure and Applied Chemistry*, 69, 979, 1997.

[99] T.; Brouwer A. M.; Verhoeven J. W. van Stokkum, I. H. M.; Scherer. *The Journal of Physical Chemistry*, 98 (3), 852, 1994.

[100] D. S.; van Grondelle R. van Stokkum, I. H. M.; Larsen. *Biochimica et Biophysica Acta*, 1657, 82, 2004.

[101] W. Satzger, H.; Zinth. *Chemical Physics*, 295 (3), 287, 2003.

[102] M.-K.; Weber I.; Glaubitz C.; Wachtveitl J. Neumann, K.; Verhoefen. *Biophysical Journal*, 94(12), 4796, 2008.

[103] I. H. M. Mullen, K. M.; van Stokkum. *Journal of Statistical Software*, 18 (1), 1, 2007.

[104] J. Snellenburg. http://glotaran.org/. *VU University Amsterdam.*

[105] Van Huong P. Lascombe, J. and Josien M.-L. *Bull. Soc. Chim. (France)*, 1175, 1959.

[106] A. D. Buckingham. *Proc. Roy. Soc. (London)*, 248A, 169, 1958.

[107] Bunger W. B. Sakano T. K. Riddick, J. A. Organic solvents: Physical properties and methods of purification, 4th edition. *John Wiley and Sons, New York*, 2, 1986.

[108] C.; Hochstrasser R. M. Anfinrud, P. A.; Han. *Proc. Nat. Acad. Sci.*, 86 (21), 8387, 1989.

[109] K. F.; Bonvalet A.; Bouzhir-Sima L.; Lambry J.-C.; Liebl U.; Joffre-M.; Vos M. H. Nuernberger, P.; Lee. *J. Am. Chem. Soc.*, 133 (43), 17110, 2011.

[110] M. L. Hush, N. S.; Williams. *J. Mol. Spectr.*, 50, 349, 1974.

[111] T. A.; Anfinrud P. A. Lim, M.; Jackson. *J. Chem. Phys.*, 102, 4355, 1995.

[112] J. E.; Jackson T. A.; Lim M.; Anfinrud-P. A. Sagnella, D. E.; Straub. *Proc. Nat. Acad. Sci.*, 96 (25), 14324, 1999.

[113] K. F.; Bonvalet A.; Vos M. H.; Joffre M. Nuernberger, P.; Lee. *J. Phys. Chem. Lett.*, 1 (14), 2077, 2010.

[114] A. Marcelli. *Private Comunication.*

[115] K.; Bouzhir-Sima L.; Lambry J.-C.; Balland V.; Vos M. H.; Liebl-U. Jasaitis, A.; Hola. *Biochemistry*, 45 (19), 6018, 2006.

[116] P. A.; Luque F. J.; Marti M. A.; Estrin D. A. Boechi, L.; Mañez. *Proteins: Structure, Function, and Bioinformatics*, 78 (4), 962, 2010.

[117] N.; Traylor T. G.; Magde D. Grogan, T. G.; Bag. *J. Phys. Chem.*, 98 (51), 13791, 1994.

[118] J.; Lee T.; Lim M. Kim, J.; Park. *J. Phys. Chem. B*, 113 (1), 260, 2008.

[119] J-C. Lambry J-L. Martin J. M. Friedman M. Guertin M. H. Vos A. Jasatis, H. Oullet. *Chemical Physics*, 396, 10, 2012.

[120] S. F. Bowne W. Doster L. Eisenstein H. Frauenfelder D. Good J. D. MCdonald M. C. Marden P. P. Moh L. Reinisch A. H. Reynolds E. Shyamsunder J. 0. Alben, D. Beece and K. T. Yue. *Proc. Natl. Acad. Sci. USA*, 79, 3744, 1982.

# Acknowledgements

It is a pleasure to thank the many people who made this thesis possible, for this reason I want to thank all the people of 'Femto Group' first of all my tutor Prof. Paolo Foggi, then Prof. Roberto Righini, Dr. Andrea Lapini, Dr. Mariangela Di Donato, Dr. Agnese Marcelli, Dr. Laura Bussotti, Dr. Manuela Lima , Alessandro Iagatti, Elena Ragnoni and Nicolò Azzaroli. A special thanks to my ex collegues Dr. Patricia Tourón Touceda and Dr. Sandra Mosquera Vásquez with whom I enjoyed at work and outside. Another special thanks to Dr. Mario Siciliani de Cumis which turned out to be a friend as well as a good colleague. I am especially grateful to my two flatmates Angelo Gallo and Serena Lorenzini for all the times in which they have comforted me after a bad day. Thanks to my boyfriend Luigi Palmieri who has always encouraged me and thanks to all my friends. The last acknowledgment is for my family for supporting me throughout my life. To them I dedicate this thesis.